Engineering Radiocatalytic Nanoliposomes with Hydrophobic Gold Nanoclusters for Radiotherapy Enhancement

Nazareth Milagros Carigga Gutierrez, Tristan Le Clainche, Anne-laure Bulin, Sofia Leo, Malika Kadri, Ahmed Gamal Ali Abdelhamid, Núria Pujol-Solé, Girgis Obaid, Marc-andré Hograindleur, Vincent Gardette, et al.

ADVANCED MATERIALS
www.advmat.de

Engineering Radiocatalytic Nanoliposomes with Hydrophobic Gold Nanoclusters for Radiotherapy Enhancement

Nazareth Milagros Carigga Gutierrez, Tristan Le Clainche, Anne-Laure Bulin, Sofia Leo, Malika Kadri, Ahmed Gamal Ali Abdelhamid, Núria Pujol-Solé, Girgis Obaid, Marc-André Hograindleur, Vincent Gardette, Benoit Busser, Vincent Motto-Ros, Véronique Josserand, Maxime Henry, Lucie Sancey, Amandine Hurbin, Hélène Elleaume, Eaazhisai Kandiah, Xavier Le Guével, Jean-Luc Coll, and Mans Broekgaarden**

Chemoradiation therapy is on the forefront of pancreatic cancer care, and there is a continued effort to improve its safety and efficacy. Liposomes are widely used to improve chemotherapy safety, and may accurately deliver high-Z element- radiocatalytic nanomaterials to cancer tissues. In this study, the interaction between X-rays and long-circulating nanoliposome formulations loaded with gold nanoclusters is explored in the context of oxaliplatin chemotherapy for desmoplastic pancreatic cancer. Hydrophobic gold nanoclusters stabilized with dodecanethiol (AuDDT) are efficiently incorporated in nanoliposomal bilayers. AuDDT-nanoliposomes significantly augmented radiation-induced •OH production, which is most effective with monochromatic X-rays at energies that exceed the K-shell electron binding energy of Au (81.7 keV). Cargo release assays reveal that AuDDT-nanoliposomes can permeabilize lipid bilayers in an X-ray dose- and formulation-dependent manner. The radiocatalytic effect of AuDDT-nanoliposomes significantly augments radiotherapy and oxaliplatin-chemoradiotherapy outcomes in 3D pancreatic microtumors. The PEGylated AuDDT-nanoliposomes display high tumor accumulation in an orthotopic mouse model of pancreatic cancer, showing promise for nanoliposomes as carriers for radiocatalytic nanomaterials. Altogether, compelling proof for chemo-radiation dose-enhancement using AuDDT-nanoliposomes is presented. Further improving the nanoliposomal loading of high-Z elements will advance the safety, efficacy, and translatability of such chemoradiation dose-enhancement approaches.

1. Introduction

Chemoradiation therapy (CRT) remains on the forefront of cancer care, playing a critical role in preventing disease recurrence in surgically resected tumors and extending the survival of inoperable patients.[1–3] For patients with locally advanced pancreatic ductal adenocarcinoma (PDAC), CRT with multi-agent chemotherapy such as FOLFIRINOX (folinic acid, fluorouracil, irinotecan, oxaliplatin) is one of the most effective treatment regimens, albeit with an overall survival of only ≈15 months post-diagnosis.[4–6] Moreover, only a small fraction of patients have a sufficient vitality score to be eligible for such combination regimens.[7] In these multi-agent CRT regimens, the chemotherapy efficacy may be limited due to an extensive desmoplastic reaction that forms a dense protective barrier of stromal cells and extracellular matrix around cancer tissues.[8–10] The high cell densities and high interstitial pressures prevent the diffusion of both molecular and nanoscale therapeutics beyond the tumor periphery,[9,11]

The ORCID identification number(s) for the author(s) of this article can be found under https://doi.org/10.1002/adma.202404605

DOI: 10.1002/adma.202404605

N. M. Carigga Gutierrez, T. L. Clainche, A.-L. Bulin, S. Leo, M. Kadri, A. G. A. Abdelhamid, N. Pujol-Solé, B. Busser, V. Josserand, M. Henry, L. Sancey, A. Hurbin, X. L. Guével, J.-L. Coll, M. Broekgaarden
Université Grenoble-Alpes
Inserm U1209
CNRS UMR 5309
Institute for Advanced Biosciences
Allée des Alpes
La Tronche 38700, France
E-mail: Jean-luc.coll@univ-grenoble-alpes.fr; Mans.broekgaarden@univ-grenoble-alpes.fr

whereas a hypoxic and immunosuppressive microenvironment contribute to radioresistance.[12]

Emerging evidence suggests that generating high amounts of reactive oxygen species (ROS) in cancer tissues can alleviate desmoplasia, increase tumor permeability, and synergize with various chemotherapeutics.[13–16] This has been demonstrated in the field of photodynamic therapy (PDT), a cancer treatment that utilizes light-induced excitation of tumor-localized dyes (i.e., photosensitizers). When excited by light, photosensitizers engage in photochemical reactions with O_2 to generate ROS (e.g., $^1O_2$). In turn, these ROS oxidize lipids, proteins, and other biological substrates, culminating in cell death.[17,18] Recent advances in the field have uncovered that PDT can improve drug penetration in cancer tissues by reducing the high cell- and collagen densities, and increase the vascular-enhanced permeability and retention (EPR) effect.[13,14,16,19–21] The combination of PDT and immediate adjuvant chemotherapy release from photosensitizer-functionalized nanoconstructs was shown to inhibit metastasis formation and enable significant chemotherapy dose reductions for efficient PDAC management in vivo.[13,22] However, the use of light to prime and increase the permeability of cancer tissues is hampered by the limited and inhomogeneous penetration depth of light in tissue.[23] Novel approaches to prime the microenvironment with deeply-penetrating X-rays could represent a substantial improvement, as these are already part of the standard-of-care for >50% of cancer patients.[24]

We hypothesize that nanoparticles composed of high-Z elements are able to increase tumor permeability by elevating radiotherapy-induced ROS production. The therapeutic mechanism of radiotherapy revolves around the direct one-electron damage to DNA bases, as well as the radiolysis of water molecules that produces highly cytotoxic hydroxyl radicals (•OH).[25] The use of high-Z elements such as gold (Z_{Au} = 79) augments these effects, as they absorb X-rays more efficiently than water and soft tissues, especially in the orthovoltage range (<250 keV).[26] The interactions of X-rays with Au atoms produce Auger- and photoelectrons that deposit their energy in the Au atom surroundings, resulting in the enhanced radiolysis of water and the associated generation of •OH.[27,28] Au nanoparticles were among the first studied radiotherapy dose-enhancement agents, showing significantly elevated survival of mice bearing subcutaneous EMT6 tumors treated with Au nanoparticles and radiotherapy (250 kVp X-rays).[29] We and others recently showed that Au nanoclusters <2 nm can catalyze ROS production and augment radiotherapy outcomes in spheroid models of glioblastoma (monochromatic 81.7 keV X-rays),[30] in vitro and in vivo models of murine breast cancer (160 kVp X-rays),[31] human subcutaneous prostate cancer (^{137}Cs γ-rays, 661 keV),[32] and murine subcutaneous cervical carcinoma (^{137}Cs γ-rays, 661 keV).[33] However, one of the main limitations of Au nanoclusters is their rapid plasma elimination half-times that results in limited tumor accumulation.[34]

Nanoliposomes (NLs) are nanoscale phospholipid vesicles that are widely to increase the bioavailability and circulation times of hydrophobic and amphiphilic compounds, and which effectively accumulate in cancer tissues through the EPR effect.[35] With the aim to augment the bioavailability and radiotherapeutic applications of Au nanoclusters, this study explored their encapsulation and radiocatalytic properties when incorporated into nanoliposomal formulations. To achieve this, the Au nanoclusters were tuned to a size range (<3 nm[36]) that is compatible with incorporation into the lipid bilayers of nanoliposomes (4–8 nm). While liposomal encapsulation of hydrophobic gold nanoclusters on the membrane properties of liposomes has been explored previously,[37–40] the evaluated formulations lacked long-circulating capabilities, and their radiotherapeutic applications have never been studied. Therefore, in this study, Au nanoclusters were incorporated in clinically relevant stealth NL formulations that are sterically stabilized with polyethylene glycol (PEG). By leveraging monochromatic synchrotron radiation, new insights toward the interactions and of Au nanocluster-loaded NLs with X-rays are presented, providing, for the first time, mechanistic evidence for their radiocatalytic properties. In vivo biodistribution studies in an orthotopic mouse model of pancreatic cancer demonstrated formidable tumor accumulation of the NLs, thus solidifying their promise for the controlled delivery of radiocatalyic nanomaterials to cancer tissues. Altogether, the findings presented here demonstrate the promising features of radiocatalytic NLs loaded with AuDDT and identify novel opportunities to further improve such approaches to enhance chemoradiotherapy.

2. Results and Discussion

2.1. Characterization of AuDDT Liposomes

Prior to liposome formation, the AuDDT nanoclusters in $CHCl_3$ were analyzed by electron microscopy and DLS, revealing two populations of nanoclusters of 0.96 ± 0.32 nm and 3.50 ± 1.2 nm (**Figure 1A,B**). The absorption spectra displayed two typical absorption bands at 413 and 680 nm of gold nanoclusters containing 25 gold atoms.[41] In $CHCl_3$ AuDDT exhibits a broad SWIR photoluminescence emission centered at 1013 nm with a quantum yield reaching 0.65%[42] (Figure 1C). AuDDT-loaded NLs with a composition of DOPE:cholestrol: DSPE-PEG (48:48:4) were prepared by lipid film hydration in PBS. Hot sonication (60 °C) was used to dissolve the lipid film and produce liposomes <200 nm. Successful liposomal incorporation was confirmed by

S. Leo
Porphychem SAS
Longvic 21600, France
G. Obaid, E. Kandiah
Department of Bioengineering
University of Texas at Dallas
Richardson, TX 75080, USA
M.-A. Hograindleur
European Synchrotron Radiation Facility
CM01 Beamline
71 Avenue des Martyrs, Grenoble 38000, France
V. Gardette, V. Motto-Ros
Université Lyon 1
Institut Lumière Matière, CNRS UMR 5306
Université de Lyon
Villeurbanne, France
V. Gardette, B. Busser, V. Motto-Ros
University Hospital of Grenoble Alpes
Grenoble 38000, France
H. Elleaume
Université de Grenoble-Alpes
Synchrotron Radiation for Biomedicine, Inserm UA07
2280 Rue de la Piscine, Saint Martin d'Hères 38400, France

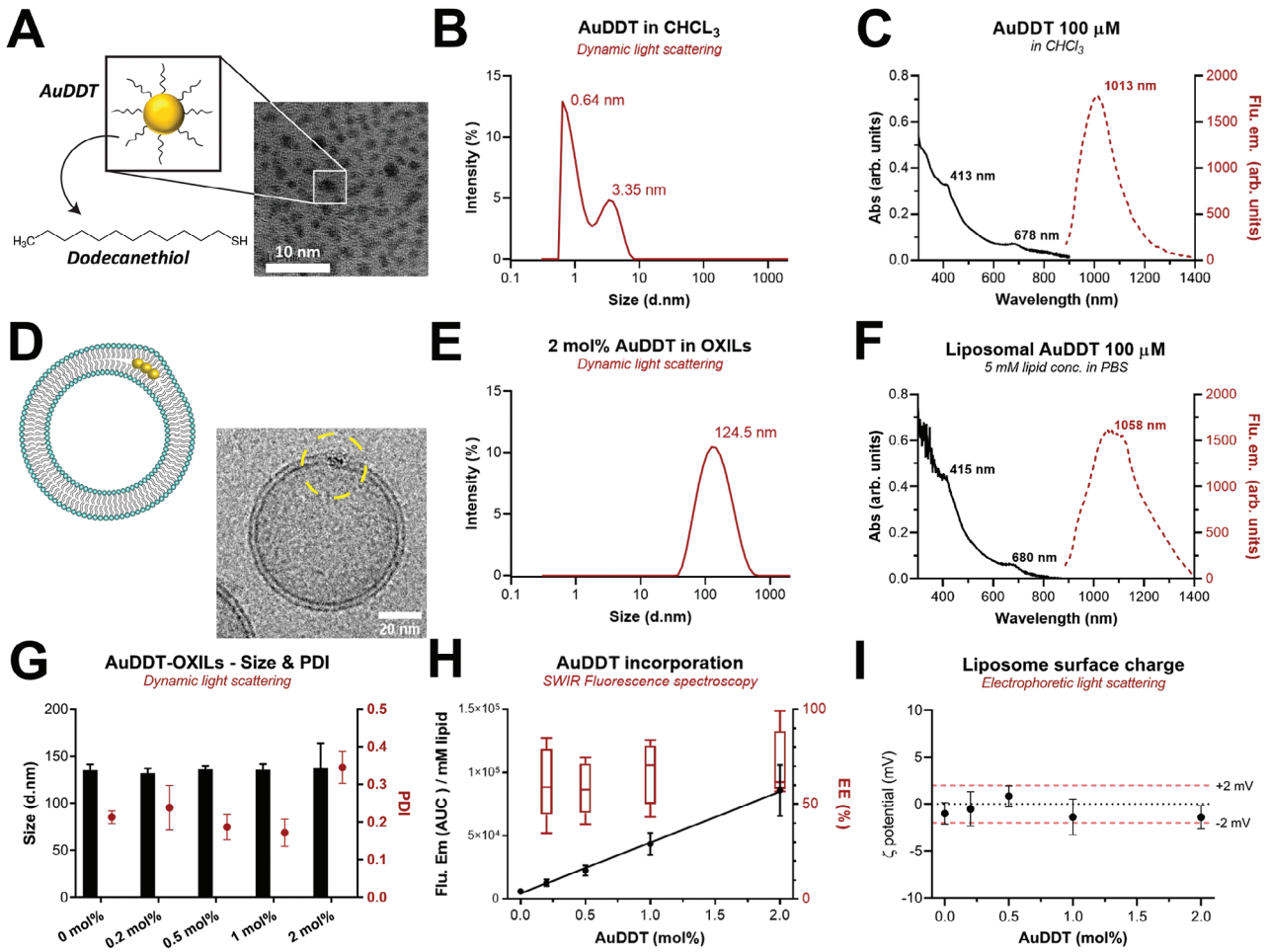

Figure 1. Characterization of AuDDT-OXILs. A) AuDDT morphology imaged by TEM microscopy and B) hydrodynamic diameters measured by dynamic light-scattering. C) Absorption (black line) and fluorescence emission spectra of AuDDT (100 µM Au in CHCl3). D) AuDDT-NLs morphology imaged by cryo-TEM and E) hydrodynamic diameter measured by dynamic light scattering spectroscopy. F) Absorption (black line) and fluorescence emission spectra of AuDDT-NLs (100 µM Au) in PBS. G) Size and polydispersity of AuDDT-NLs at different Au: lipid ratios. H) Semi-quantitative encapsulation efficiencies (EE%) of AuDDT at varying molar ratios in NLs (box whisker plots depict the mean, 25th and 75th percentile, and the 95% CI). I) Effect of AuDDT on NLs ζ-potentials. All data was obtained from $N \geq 9$ from ≥ 3 technical repeats.

cryo-TEM, as electron-dense regions in the lipid bilayer could be observed (Figure 1D) that were consistent in size with the TEM images of AuDDT (Figure 1A) and previous observations.[40,43,44] The inclusion of AuDDT did not affect the size or polydispersity of liposomes: The liposomes were ≈130 nm with a polydispersity index (PDI) <0.2 (Figure 1E,G). The exception was liposomes containing 2 mol% AuDDT, for which the PDI was 0.34. The absorption spectra of AuDDT-OXILs, corrected for empty OXILs, were globally similar to free AuDDT in $CHCl_3$, with distinct bands at 413 and 680 nm (Figure 1F). The emission spectra exhibited a substantial alteration compared to free AuDDT in $CHCl_3$ with a bathochromic shift of the maximum peak emission at 1058 nm (Figure 1F). Desiccating and reconstituting the AuDDT-NLs in $CHCl_3$ restored their fluorescence emission spectra, and enabled the quantification of the encapsulation efficiencies (EE%), which was ≈70% across all Au: lipid ratios (Figure S1C, Supporting Information). This correlated well with a semi-quantitative approach based on the maximum fluorescence emission intensity of AuDDT-NLs in PBS (1058 nm) compared to that of native AuDDT in $CHCL_3$ (1013 nm) (Figure 1H). Interestingly, quantification of the encapsulation efficiency by measuring elemental Au by ICP-MS yielded a 100% encapsulation efficiency (Figure S1J, Supporting Information). The slight loss in AuDDT emission was therefore attributed to the reported aggregation of gold nanoparticles by sonication,[45,46] leading to visible sediments that could be removed by centrifugation. The encapsulation of AuDDT did not affect the liposome surface charge, which remained neutral within a range of −2 and +2 mV (Figure 1I). Nanoparticle tracking analysis did reveal an AuDDT-concentration-dependent increase in light scattering, which plateaued > 1 mol% Au (Figure S1D, Supporting Information).

2.2. AuDDT Localizes within Lipid Bilayers and Forms Aggregates in a Concentration-Dependent Manner

The localization of AuDDT within the NLs was investigated using cryo-TEM at varying Au: lipid ratios, expressed as mol%

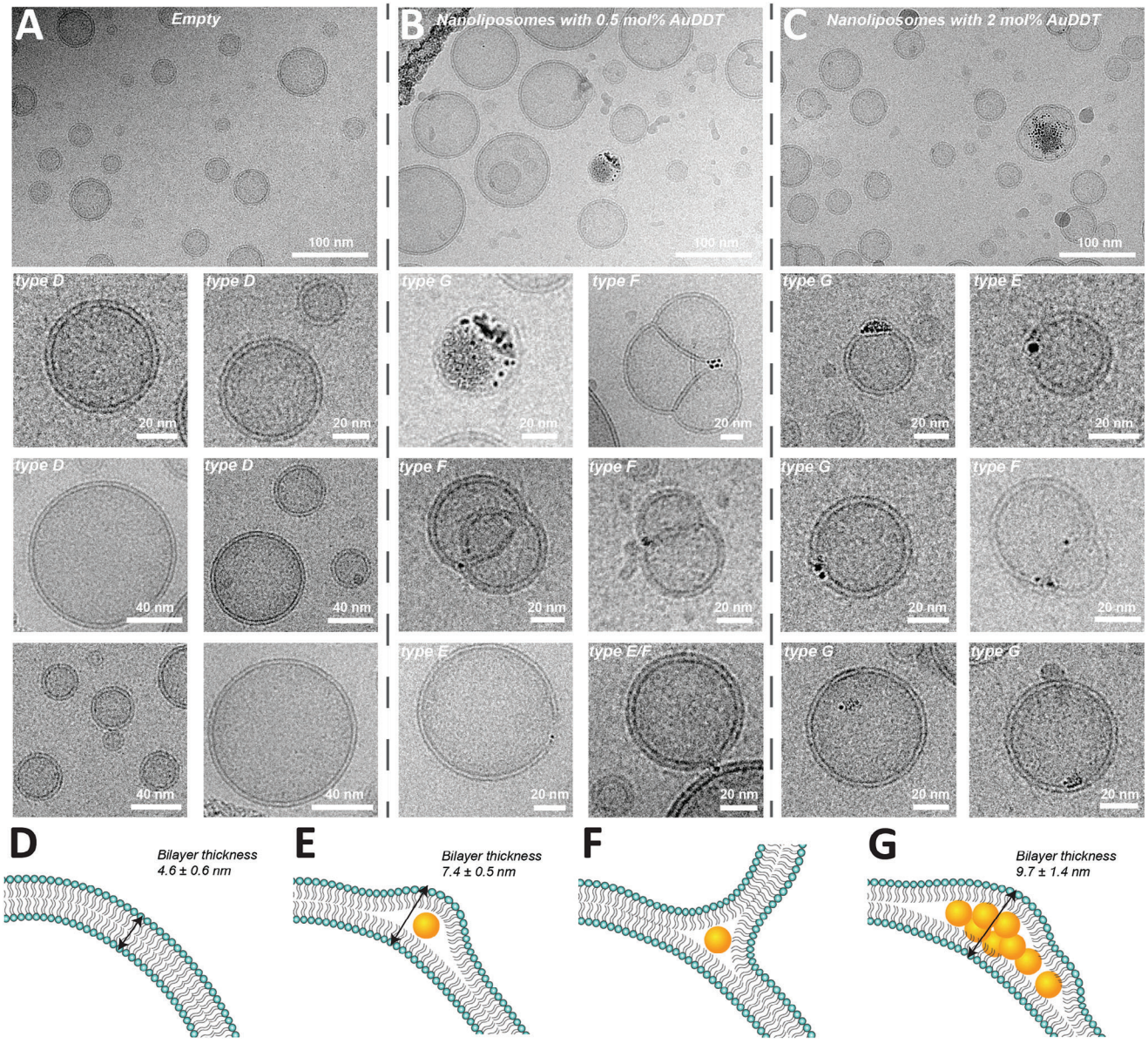

Figure 2. Cryo-electron microscopy analysis of AuDDT-NLs reveals single nanoclusters and aggregate formation within lipid bilayers. Depicted images were obtained of empty NLs (A), NLs containing 0.5 moL% AuDDT (B), or NLs containing 2 moL% AuDDT (C). Four types of liposomes were observed, containing either no nanoclusters (D), NLs with a single AuDDT that pushed apart the inner and outer membrane leaflet (E), NLs containing a single AuDDT or aggregated AuDDT that caused lipid bilayer fusion (F), and, G) NLs containing aggregates of nanoclusters between the membrane leaflets.

Au. In the absence of AuDDT, the liposomes were relatively homogeneous unilamellar vesicles with an average bilayer thickness of 4.6 ± 0.6 nm (**Figure** 2A). While the images are top–down projections of the 3D liposomes, the presence of AuDDT in the lipid bilayer was frequently observed for all AuDDT-NLs (Figure 2B,C; Figure S2, Supporting Information). In the images, a variety of AuDDT-NLs types were observed. First, the majority of the NLs did not appear to contain AuDDT at all molar percentages (type Figure 2D). Although observed for all AuDDT-NLs, vesicles containing single AuDDT nanoclusters (type 2E) were most frequently observed in AuDDT-NLs with 0.2 mol% Au (Figure S2B, Supporting Information). The maximum bilayer thickness at such events was quantified at 7.6 ± 0.5 nm, indicating that AuDDT pushes apart the inner and outer membrane leaflets. Such liposomes appeared to be susceptible to fusion, as multi-vesicular AuDDT-NLs were frequently observed with a single- or cluster of AuDDT at the intersections of the lipid bilayers (Figure 2F). Previous studies demonstrated that slightly bigger AuDDT (3 and 5 nm, stabilized by either DDT or stearic acid) included in dipalmitoyl-phosphatidylcholine:dipalmitoyl-phosphatidylglycerine liposomes (DPPC: DPPG, 85:15) led to local bilayer softening.[43,44] This phenomenon may lie at the basis for the NLs fusions observed in our formulations, and which may be enhanced by the properties of fusogenic properties of

DOPE.[47] These properties stem from the relatively small PE headgroup relative to its hydrophobic tails, which promote the formation of H_{II}-inverted micelles.[48] Cholesterol was also included with the purpose of increase membrane fluidity, improve AuDDT encapsulation, and increase the bilayer stability and barrier function.[49] However, through increased membrane fluidity and promoting curvature flexibility, cholesterol may also promote the fusion of lipid bilayers.[50] In dispersions of AuDDT-NLs with 0.5 and 2 mol% Au, hyper-loaded AuDDT-NLs were frequently observed (type Figure 2G). In such NLs, the maximum thickness of the bilayer was observed to stretch to 9.7 ± 1.4 nm. It is worth noting that extraliposomal aggregates of AuDDT clusters were only observed once in 560 images in the 2 mol% AuDDT-NLs sample (Figure S2, Supporting Information). To ascertain the exact localization of AuDDT within the lipid bilayers with absolute confidence, cryo-electron tomography was performed (Videos S1–S3, Supporting Information), from which two important observations were made. First, AuDDTs that were highly in focus were exclusively located within lipid bilayers or at lipid bilayer intersections during liposome fusion events. Second, while only a few AuDDT-positive were observed in typical cryo-TEM micrographs, the cryo-electron tomography illustrates that the majority of liposomes contained one or more AuDDT.

When assessing the size and polydispersity of the nanoliposomes immediately after the preparation, satisfactory results were obtained (Figure 1G). This indicates that the liposome formation is not negatively impacted in the presence and insertion of AuDDT into the lipid bilayers and that the multilamellar vesicles are not emerging at this step. To determine whether fusion events occur during the storage process, we analyzed the liposome size and polydispersity again at 2 and 4 weeks post-preparation. These results show that the liposomes largely retain their size and polydispersity in this time period, but a trend toward increased particle size, polydispersity, and reduced particle numbers indeed suggest that fusion events occur during prolonged storage (Figure S1, Supporting Information, panels G–I). We, therefore, hypothesize that a storage period prior to Cryo-TEM, together with the fusogenic properties of DOPE and the lamellar extending effects of AuDDT, may have given rise to the multilamellar vesicles depicted in Figure 2 and Figure S2 (Supporting Information). Across all NLs with varying AuDDT molar ratios, 80.2% of the observed NLs were classified as unilamellar vesicles, 10.4% as fused unilamellar vesicles, and 9.2% as multilamellar vesicles. No significant differences were observed between NLs loaded with different molar ratios of AuDDT. In contrast, the number of NLs that contained AuDDT was different for the various molar ratios included. At 0.2 mol% AuDDT, 50.2% of the NLs contained single clusters and 7.0% contained small AuDDT aggregates. A lower amount of AuDDT-NLs were observed at higher molar ratios, namely 21.5% single clusters and 8.3% small aggregates for 0.5 mol% AuDDT-NLs, and 25.7% of NLs contained single clusters and 6.6% of small aggregates for 2 mol% AuDDT-NLs. However, due to the small size of the AuDDT, any clusters that are out-of-focus may have been missed in this quantification.

Additional SAXS analysis was performed to characterize the AuDDT-NLs. From the low-Q range of the spectra, a general increase in X-ray scattering was observed for the AuDDT-NLs in comparison to the empty NLs, confirming the presence of AuDDT in the vesicles. The Guinier radius was determined at 651.51 ± 52.68 Å and 654 ± 57.11 Å for empty NLs and AuDDT-NLs, respectively, which confirmed the results obtained with DLS. The overall bilayer thickness was estimated by the maxima in the high-Q range, which yielded an overall bilayer thickness of 8.36 nm for AuDDT-NLs, versus 7.54 nm for empty NLs. This confirms our findings of bilayer thickening upon the inclusion of AuDDT by pushing apart the lamellar structure of the NLs. The minor difference is likely the result of only a few AuDDT insertion events per NL.

These findings are well-aligned with previous studies in which a similar heterogeneous loading of AuDDT was observed in liposomes composed of DPPC: DPPG.[43] This has been attributed to the non-homogenous formation of lipid-AuDDT films during the preparation procedure.[37,43] More homogeneous AuDDT-lipid films may be formed via a $CHCl_3$-annealing step prior to lipid-film hydration, yet the resulting entrapment of $CHCl_3$ molecules in the bilayer could negatively impact their biocompatibility.[37] The findings presented here are the first evidence that AuDDT can also be encapsulated in NLs with a stealth-like formulation that contained DPSE-PEG and cholesterol, which are frequently used in clinical liposome compositions.[51]

2.3. AuDDT-Liposomes Exhibit Radiocatalytic Properties in a Au-Dependent Manner

The radiation dose-enhancing properties of Au are believed to stem predominantly from its increased interaction with X-rays compared to soft tissues,[26] which produces elevated levels of secondary electrons and photons in an X-ray energy-dependent manner (**Figure 3**A). To quantify these effects, Monte Carlo simulations were performed using X-rays tuned 1 keV below and above the K-shell electron binding energy of Au (i.e., 80.7 keV, Figure 3B,C), where the mass energy absorption coefficient exhibits a sharp increase compared to soft tissues and water (Figure 3D). The results demonstrate that Au produces high amounts of secondary electrons in comparison to water (Figure 3B,C). Below the K-edge of gold, high-energy photoelectrons are generated as the incoming X-rays interact with the KM_5-KL_1 shells (<14 keV), the L_1–L_3 shells (>65 keV), and the M_1–M_5 shells (69–78 keV) (Figure 3B). Above the K-edge of Au, similar photoelectrons are generated, in addition to a distinct peak of Auger-electrons between 50–55 keV (Figure 3C). These are generated due to the emission of 1 keV photoelectrons from the K-shell, and the subsequent recombination with L-shell electrons.[52] At both X-ray energies, typical Compton scattering spectra can be observed: <18.9 keV for 79.7 keV, and <19.8 keV for 81.7 keV X-rays. These spectra contrast with those observed when X-rays interact with water molecules, which almost exclusively produce electrons generated by Compton scattering (Figure 3D,E). The generation of secondary photons was similarly investigated (Figure S3, Supporting Information): Irradiation of Au produced lower amounts of high-energy photons compared to water (>60 keV) which are the result of inelastic Compton diffusions on atomic electrons. In contrast, there are higher amounts of low-energy photons (17 keV) being emitted from Au compared H_2O, which corresponds to the X-ray fluorescence emission by Au.

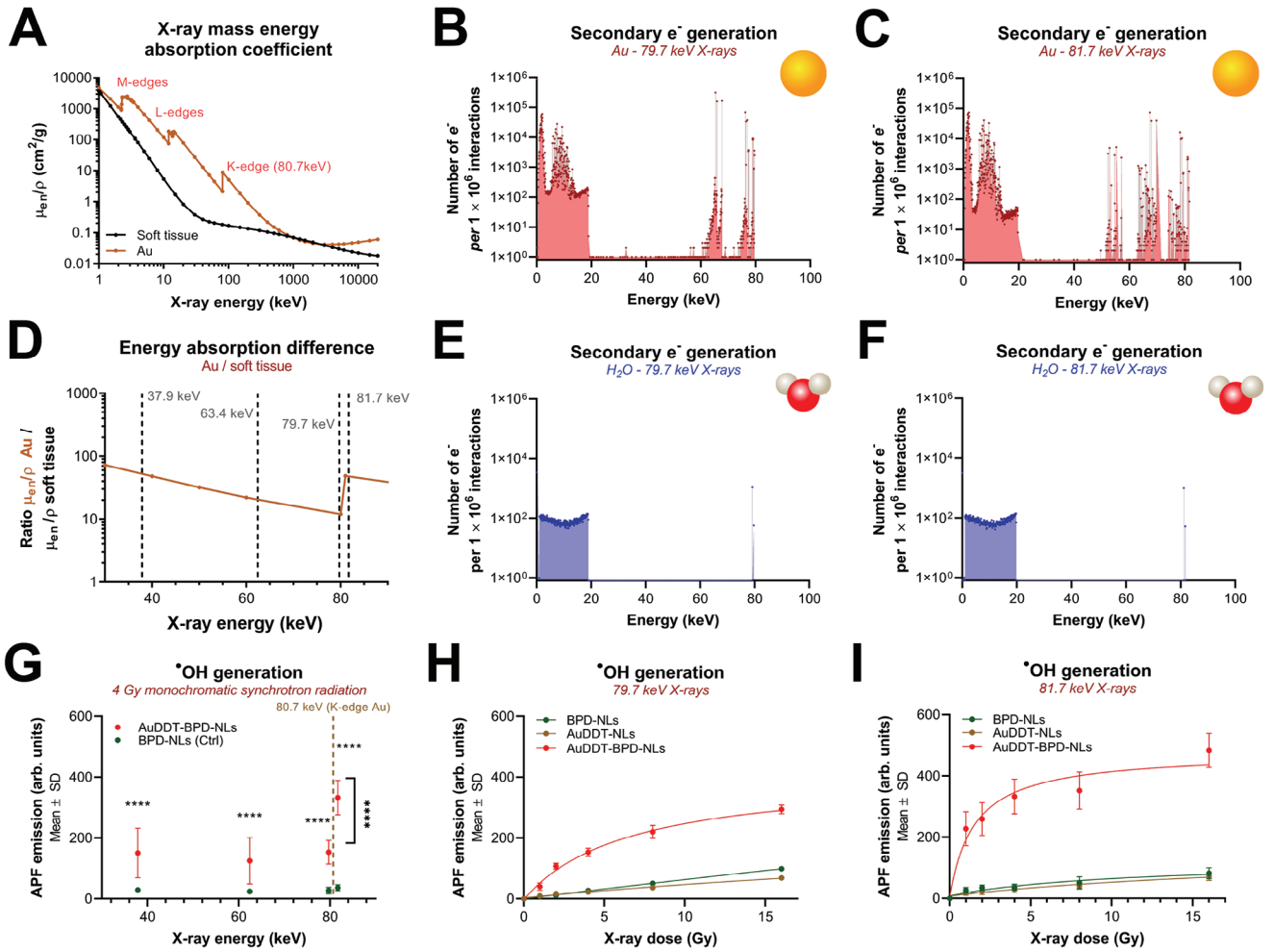

Figure 3. X-ray interactions with Au increases the generation of secondary electrons and elevates hydroxyl radical formation. A) The X-ray mass energy absorption coefficient was plotted as a function of X-ray energy for Au and soft tissue. Simulated secondary electron spectra obtained when 79.7 keV X-rays (B) and 81.7 keV X-rays (C) interact with Au. D) Ratio of the mass energy absorption coefficients of Au and soft tissue, plotted as a function of the X-ray energy. Indicated in gray are the X-ray energies selected for the APF oxidation assays. Simulated secondary electron spectra obtained when 79.7 keV X-rays (E) and 81.7 keV X-rays (F) interact with water. G) APF oxidation by monochromatic synchrotron radiation in the presence of NL containing only BPD (BPD-NLs, dark green, control), or AuDDT-BPD-NL (red). Data was analyzed using a One-way ANOVA and Sidak's multiple comparisons test. APF oxidation as a function of X-ray dose in the presence of BPD-NLs (green), AuDDT-NLs (gold), and AuDDT-BPD-NLs (red), under X-ray energy of either 79.7 keV (H) or 81.7 keV (I). Data was fitted using an agonist versus response (three-parameter) fit.

To determine whether such phenomena could lead to increased radiolysis of water molecules, an initial AuDDT-NL formulation of DOPC: DSPE-PEG (98:2 mol%) was prepared and exposed to monochromatic synchrotron radiation in the presence of the •OH sensor APF. As it was previously reported that gold nanoparticles and BPD exhibited radiocatalytic synergy under 6 MVp X-ray irradiation,[53] NLs containing either 0.8 mol% BPD alone (BPD-NLs, controls), 0.5 mol% AuDDT (AuDDT-NLs), and AuDDT-BPD-NLs were synthesized and evaluated. SAXS analysis confirmed that BPD had no overall influence on the size, or bilayer thickness compared to empty NLs and AuDDT-NLs (Figure S2E–H, Supporting Information). The mean bilayer thickness was estimated by SAXS to be at 7.50 nm, and 9.1 nm for BPD-NLs and AuDDT-BPD-NLs, respectively. The oxidation of APF was investigated upon exposure to monochromatic synchrotron radiation tuned at 37.9, 62.4, 79.7, and 81.7 keV, the latter being 1 keV above the K-shell electron binding energy of Au (Figure 3D). The results show that APF oxidation in the presence of BPD-NLs and AuDDT-NLs occurred in a dose-dependent manner (Figure 3G–I). In comparison, APF oxidation by AuDDT-BPD-NLs was significantly higher at all X-ray energies. Irradiation with X-rays tuned 1 keV above the K-shell electron binding energy of Au (81.7 keV) resulted in significantly elevated APF oxidation compared to 79.7 keV, indicating that •OH generation is driven by the X-ray-interactions with Au (Figure 3G).

The finding that BPD significantly elevated ROS production was surprising, for which an average synergy index across all radiation doses was 1.42 ± 0.08. Whereas previous studies on the synergistic radiocatalytic behavior of water-soluble Au nanoparticles and membrane-embedded BPD were performed with 6 MVp X-rays, a contribution by Cerenkov radiation that overlaps with the UV absorption of porphyrins (Soret band) could

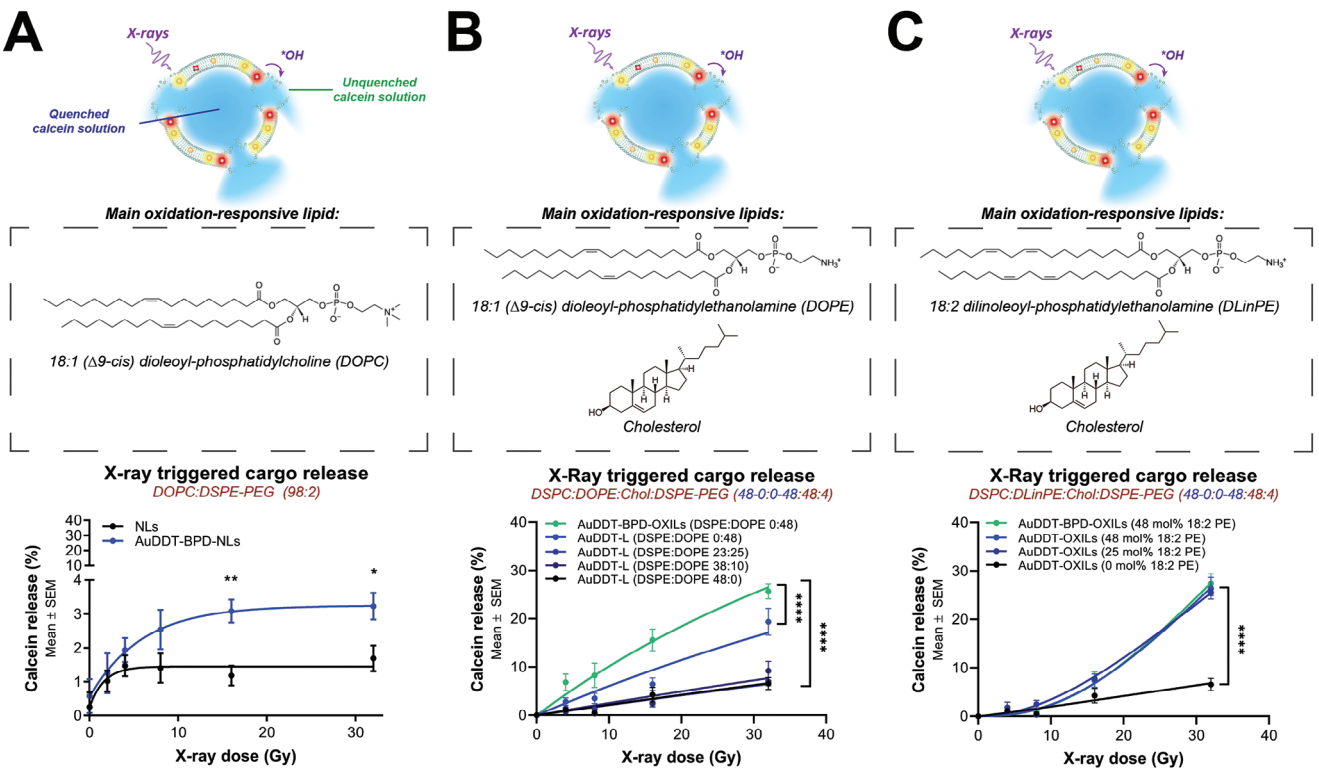

Figure 4. Cargo-release from AuDDT-BPD-OXILs occurs in a formulation-dependent manner. A) X-ray-triggered cargo release from AuDDT-BPD-NLs composed of DOPC: DSPE-PEG (98:2 mol%) upon irradiation with 81.7 keV monochromatic synchrotron radiation. Data represents $N = 9$ from three technical repeats. B) X-ray-triggered cargo release from AuDDT(-BPD)-OXILs composed of increasing DOPE content (0–48 mol% at the expense of DSPC (48–0 mol%), and further supplemented with cholesterol (48 mol%) and DSPE-PEG (4 mol%). Cargo release was induced upon irradiation with 81.7 keV monochromatic synchrotron radiation. Data represents $N = 12$–20 from four technical repeats. C) X-ray-triggered cargo release from AuDDT (-BPD)-OXILs composed of increasing DLinPE content (0–48 mol% at the expense of DSPC (48–0 mol%), and further supplemented with cholesterol (48 mol%) and DSPE-PEG (4 mol%). Cargo release was induced upon irradiation with 81.7 keV monochromatic synchrotron radiation. Data represents $N = 8$–10 from three technical repeats. All data was fitted using agonist versus normalized response fits, and curves were statistically compared using an extra sum-of-squares *F*-test.

be considered.[54] However, such events do not occur at ortho-voltage X-rays (<220 keV)[55] and therefore cannot explain the observed findings. We therefore hypothesize the synergy stems from the reducing power of porphyrins, which have been reported to be strong reducing agents that can readily donate electrons.[56] In conjunction with the AuDDT nanoclusters, the Compton effect, and in particular the photoelectric and subsequent Auger events, can give rise to a loss of electrons[57] that causes Au atoms to become hyper-ionized. BPD may donate electrons to these Au atoms, forming oxidized BPD in the process. BPD may therefore act as a key intermediate in translating the physical effects of radiation dose-enhancement to biochemical redox reactions, which is supported by the findings in Figure 3B,C.

2.4. AuDDT-Enhanced Radiocatalysis Induces Membrane Leakage of Nanoliposomes in a Formulation-Dependent Manner

The consequences of the AuDDT-radiocatalyzed ROS production on lipids and lipid bilayer function were investigated, as these may play critical roles in the radiotherapeutic properties of the AuDDT-NLs. The ability of AuDDT to cause membrane permeability upon X-ray exposure was evaluated by loading the NLs with a self-quenching and iso-osmolar calcein solution, of which its release can be quantified by an increase in its fluorescence intensity. The formulation evaluated in Figure 3, composed of DOPC: DSPE-PEG (98:2 mol%) with 0.5 mol% of AuDDT and 0.8 mol% BPD released a mere 3.2 ± 0.4% of its cargo, which was nonetheless significantly higher than liposomes devoid of AuDDT and BPD (1.5 ± 0.2%, **Figure 4A**). To generate a model system that is more prone to disruption, DOPC was replaced by DOPE. In comparison to DOPC, DOPE has a smaller headgroup and assumes a conical shape that is prone to destabilize the lipid bilayers.[47,58] This was first evaluated using a photodynamic approach to generate ROS by leveraging the presence of BPD within the NLs (Figure S4A, Supporting Information). Indeed, a significantly increased cargo release was observed when DOPC was replaced by DOPE in the lipid bilayer (Figure S4B, Supporting Information). Earlier studies also indicated that cholesterol may be pivotal in causing membrane leakage upon exposure to photodynamically-generated ROS.[59] Those findings were confirmed, as cargo leakage from NLs was enhanced in a cholesterol-concentration-dependent manner (Figure S4C, Supporting Information).

Based on these findings, a new formulation was developed that was composed of DOPE:cholesterol: DSPE-PEG (48:48:4),

and which will be referred to as oxidation-responsive nanoliposomes (OXILs) from here onward. To investigate the influence of unsaturated DOPE on the lipid membrane integrity, a range of AuDDT-OXILs was prepared in which increasing amounts of DOPE were replaced by the saturated DSPC. The cargo-release results in Figure 4B revealed that cholesterol, even in the absence of unsaturated lipids, improves the cargo-release efficiency to 6.6 ± 4.4% at a dose of 32 Gy. The inclusion of 10 mol% DOPE and 25 mol% DOPE did not result in significantly increased cargo release upon X-ray irradiation (9.2 ± 7.9% and 7.0 ± 3.3%, respectively). When replacing all DSPC by DOPE, a significantly increased cargo release efficiency was observed (19.4 ± 11.2%), which was further augmented when the AuDDT-OXILs were supplemented with BPD (25.7 ± 6.1%). Significantly different EC_{50} values could be extracted from the dose-response fits, indicating irradiation doses at which 50% of the cargo could be released. These EC_{50} values were 88.5 Gy (95% CI 76.43 to 103.9 Gy) for AuDDT-BPD-OXILs (48 mol% DOPE) and 154.7 Gy (95% CI 132.3 to 184.6 Gy) for AuDDT-OXILs (48 mol% DOPE, no BPD), respectively. Next, the sensitivity of bilayers containing poly-unsaturated phospholipids was investigated. When replacing DOPE by 18:2 DLinPE, the maximum cargo release was further enhanced to a maximum of 31.2% for AuDDT-OXILs and 35.6% for AuDDT-BPD-OXILs, at 32 Gy. Notably, no significant differences between AuDDT-OXILs and AuDDT-BPD-OXILs were observed for these membrane formulations.

Lipid bilayers containing a combination of cholesterol and unsaturated lipids are most susceptible to the radiocatalytic properties of AuDDT and BPD. This warrants further investigation toward the radiotherapeutic properties of the AuDDT-BPD-OXILs on cancer models, where necrosis may be expected following tumor uptake and potential intracellular re-distribution of AuDDT to cellular membranes. Moreover, these findings are of particular interest for X-ray-controlled drug release. Although not further explored here, the AuDDT-BPD-OXIL formulation composed of DOPE:cholesterol: DSPE-PEG (48:48:4) holds potential for radiotherapy-controlled release of chemotherapeutics, and was therefore selected for in vitro investigations.

2.5. Radiation Dose-Enhancement by AuDDT-Liposomes in Pancreatic Microtumors

To investigate the radiotherapeutics properties of AuDDT-BPD-OXILs, an experimental timeline was designed in which pancreatic microtumors composed of either MIA PaCa-2 or PANC-1 cells and the addition of pancreatic stellate cells (HPSC) were seeded on day 1, underwent radiotherapy on culture day 4, and were analyzed on culture day 11. When radiotherapy was performed using 81.7 keV monochromatic synchrotron radiation, MIA-PaCa-2-HPSC microtumors exhibited high resistance, as there were no significant decreases in spheroid size or viability at 7 days post-treatment (**Figure 5**A–C). In the presence of AuDDT-BPD-OXILs, there was a notable decrease in the normalized viability, decreasing significantly by 33.6 ± 9.4% at 4 Gy (Figure 5B). The most prominent effects were observed when quantifying the microtumor size, in which significant reductions of 50.7 ± 3.0% and 31.6 ± 13.5% were observed at 4 and 16 Gy, compared to radiotherapy alone (Figure 5A,C). To determine whether the radiotherapy efficacy was increased due to a radiation-dose-enhancement effect, a second set of experiments was performed during which the microtumors were irradiated at 79.7 keV, that is, 1 keV below the K-edge of Au, and received a dose of 4 Gy. Analysis of microtumor viability indicated that irradiation at 81.7 keV resulted in a near-significant reduction in viability of 14.6 ± 12.1% compared to irradiation at 79.7 keV (Figure 5D). A more substantial difference was observed upon analysis of spheroid size, where irradiation at 81.7 keV resulted in a significant 40.2 ± 3.7% reduction in microtumor size compared to irradiation at 79.7 keV.

In microtumors composed of PANC-1+HPSC, 81.7 keV radiotherapy resulted in significant decreases in viability, yet not in microtumor size (Figure S5A–C, Supporting Information). These findings are somewhat contradictory to the observed effects in MIA PaCa-2+HPSC microtumors, but such differences between models has been observed previously.[30,60,61] AuDDT-BPD-OXILs increased the radiotherapy efficacy by further reducing microtumor viability by 30.8 ± 17.3% at 4 Gy and 20.6 ± 7.7% at 16 Gy. A minor, yet significant, increase in microtumor size caused by AuDDT-BPD-OXILs was observed at 16 Gy, which was attributed to the presence of dislodged cells from the edge of the microtumors (Figure S5C, Supporting Information). Irradiation at 81.7 keV was significantly more effective at reducing microtumor viability compared to 79.7 keV (Figure S5D, Supporting Information), whereas only minor effects were observed on microtumor size.

The physical and chemical mechanisms by which radiotherapy outcomes are enhanced by gold nanoparticles have been fairly well-established. Following ionization events stemming from Compton-, photoelectric-, or Auger effects, a high dose of energy is deposited in the vicinity around the nanoparticle. The majority of the energy is deposited within 20 nm of the particle core, but high energy photo- and/or Auger electrons >50 keV can travel up to 300 nm from where they are generated.[57] Since a single photoelectric effect may give rise to abundant Auger electrons,[57] we speculate that the resulting hyperionized Au atoms also exert biochemical oxidation reactions due to a high reduction potential. However, the extent to which these phenomena augment radiotherapy outcomes is convoluted due to a variety of biological radiotherapy-enhancing effects, although the exact effects were shown to be particle, cell-type-, and cell-line-dependent. As recently reviewed, Au nanoparticles are capable of elevating oxidative stress even in the absence of radiation. Following exposure to ionizing radiation, cancer cells typically exhibit increased oxidative stress, DNA damage, and impaired DNA damage repair, ultimately culminating in apoptotic and necrotic cell death.[62] However, these findings refer exclusively to water-soluble Au nanoparticles or AuNC.

In this context, this study is the first to evaluate the radiotherapy-enhancing effects of hydrophobic AuDDT. The presented results from distinct types of pancreatic microtumors in Figure 5 and Figure S5 (Supporting Information) convincingly demonstrate that AuDDT-BPD-OXILs increase radiotherapy efficacies via a physical Au-dependent radiocatalyic effect. We hypothesize that the fusogenic nature of the OXILs, with DOPE as a major excipient, and the non-anchored nature of AuDDT facilitates the transfer of the nanoclusters to the cellular membranes. Ionization of the Au atoms in AuDDT would then

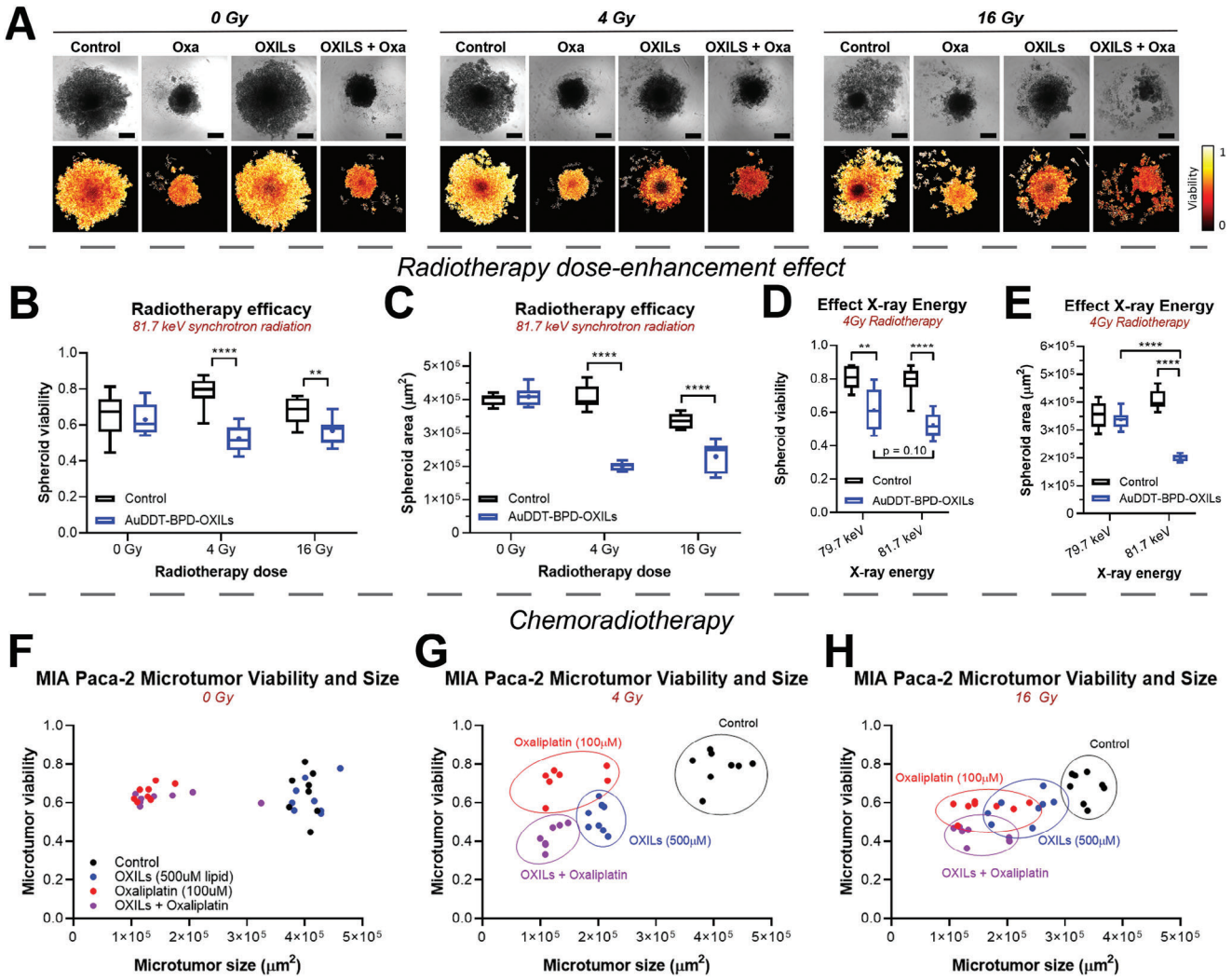

Figure 5. The radiocatalytic effects of AuDDT-BPD-OXILs enhance radiotherapy outcomes on pancreatic microtumors composed of MIA PaCa-2 and HPSC cells. A) Representative brightfield images and viability heatmaps of pancreatic microtumors following exposure to monochromatic synchrotron radiation (81.7 keV) in the presence/absence of oxaliplatin (scalebar = 500 μm). B,C) The efficacy of radiotherapy in the absence (black) and presence of AuDDT-BPD-OXILs (blue) based on microtumor viability (B) and microtumor size (C). D,E) Radiosensitization by AuDDT-BPD-OXILs was confirmed by viability assessment (D) and microtumor size quantification (E) following monochromatic X-rays tuned below (79.7 keV) and above (81.7 keV) the K-edge of Au (80.7 keV). F–H) Integrated comparison of microtumor size and viability of following chemoradiotherapy at 0 Gy (F), 4 Gy (G), and 16 Gy (H), given with 81.7 keV X-rays. Treatment groups were radiotherapy alone (black), AuDDT-BPD-OXILs + radiotherapy (blue), oxaliplatin + radiotherapy (red), and AuDD-BPD-OXILs + oxaliplatin + radiotherapy. All box-whisker plots depict the mean, 25th, and 75th percentile, and the 95% confidence interval from $N = 8$. Data passed normality tests (Pearson-Omnibus test), and statistical analyses were performed using a One-way ANOVA and Sidak's post-hoc test for multiple comparisons (asterisks), or using a student's *t*-tests between two defined groups (hashtags).

result in highly localized ionization events within a few nm of the particle surface.[57] Therefore, the therapeutic mechanism of action of AuDDT may be similar to observations in the field of photodynamic therapy, where hydrophobic porphyrin-like photosensitizers also accumulate in cellular membranes.[63] In this scenario, the photochemically produced ROS have a similarly short action radius of several nm.[64] When extrapolating the sequence of events after photodynamic therapy, we hypothesize that AuDDT-enhanced radiotherapy also leads to (phospho)lipid oxidation, loss of cell membrane integrity, and necrosis. This hypothesis deserves further investigation but is supported by the data in Figure 4.

The toxicity of empty nanoliposomes, BPD-NLs, AuDDT-NLs, and AuDDT-BPD-NLs was also evaluated on primary human pancreatic stellate cells (HPSC) and human embryonic kidney (HEK 293) cells. The results demonstrate that none of the nanoliposomes exhibited toxicity toward primary HPSC up to lipid concentrations of 2.5 mM (Figure S3D, Supporting Information). Both empty NLs and AuDDT-NLs exhibited no toxicity to human embryonic kidney cells up to concentrations of 2.5 mM, yet the formulations that contained BPD exhibited substantial toxicity to this cell line with a fitted IC50 value of 0.4 ± 0.1 mM (BPD-NLs), and 0.7 ± 0.1 mM (AuDDT-BPD-NLs, Figure S3E, Supporting Information). These findings are in support of those in Figure 5B

and Figure S5B (Supporting Information), where no toxicity of the AuDDT-BPD-NLs was observed in the different pancreatic microtumors.

2.6. AuDDT-BPD-OXIL Improves Oxaliplatin-Chemoradiation Therapy Outcomes in MIA PaCa-2-HPSC Microtumors

The efficacy of the combination therapy of radiotherapy and oxaliplatin was evaluated as it constitutes a clinically relevant approach for PDAC, with oxaliplatin being a prominent component in FOLFIRINOX and NALIRIFOX regimens.[6,65] To clearly distinguish the radiocatalytic effects of the AuDDT-BPD-OXILs from a similar effect stemming from the high-Z Pt atoms present in oxaliplatin ($Z_{Pt} = 78$), the chemotherapeutic was added immediately after irradiation rather than prior. In the absence of radiation, oxaliplatin significantly inhibited microtumor growth, resulting in 68.1 ± 5.9% smaller masses compared to the untreated controls (Figure 5F). Although there was a significant growth inhibition, oxaliplatin alone did not affect microtumor viability, indicating that it is inefficient to eradicate cancer cells as a standalone therapy. In combination with radiotherapy, oxaliplatin neither facilitated further growth inhibition, nor reduced microtumor viability compared to the microtumors subjected to radiotherapy alone (Figure 5F–H). In the absence of radiation, the AuDDT-BPD-OXILs did not exhibit toxicity by themselves, and neither enhanced the effects of oxaliplatin. However, oxaplatin chemoradiotherapy was significantly enhanced in the presence of AuDDT-BPD-OXILs, resulting in 16.0 ± 12.1% smaller and 39.6 ± 8.9% less viable microtumors compared to oxaliplatin chemoradiotherapy given at 4 Gy. These effects are best observed at 4 Gy, whereas the differences are smaller at 16 Gy, namely a non-significant 4.9 ± 14.6% reduction in size and a significant 25.4 ± 4.8% less viable microtumors compared to oxaliplatin chemoradiotherapy. These findings are encouraging when considering stereotactic radiation therapy in which individual irradiations with doses between 5–10 Gy are repetitively performed on patients with pancreatic cancer.[66] The beneficial outcomes of oxaliplatin-chemoradiotherapy with AuDDT-BPD-OXILs may stem from an additive effect of augmented oxidative stress and growth inhibition.[67,68] However, elevated ROS production by the radiocatalytic effects of AuDDT-BPD-OXILs may also have contributed to increase microtumor permeability, as will be discussed further below.

2.7. Oxaliplatin-Chemoradiotherapy Disrupts the Integrity of PANC-1-HPSC Microtumors

PANC-1-HPSC microtumors responded remarkably different to oxaliplatin chemoradiotherapy compared to the MIA PaCa-2-based model. Primarily, the PANC-1+HPSC were more susceptible to oxaliplatin chemotherapy, evidenced by a mean normalized viability of 0.30 ± 0.05 compared to 0.65 ± 0.04 for MIA PaCa-2+HPSC ($p < 0.0001$). Oxaliplatin caused substantial degradation of the PANC-1+HPSC microtumors, resulting in a complete absence of a recognizable microtumor mass at 16 Gy (Figure S5A, Supporting Information). Consequently, the analysis of microtumor size was heterogeneous and relatively non-informative. The individual tumor cell clusters still displayed signs of viability, albeit relatively low (30.2 ± 4.2%, Figure S5A,F, Supporting Information). In terms of viability, the chemoradiotherapy combined with AuDDT-BPD-OXILs displayed higher levels of viability (48.6 ± 0.13%) compared to the oxaliplatin-chemoradiotherapy (30.2 ± 4.2%) and AuDDT-BPD-OXILs + radiotherapy (30.9 ± 3.0%) groups (Figure S5A,F, Supporting Information). The origin of this discrepancy between the two models remains elusive. Differences in treatment susceptibility may lie in the metabolic phenotype of these cancer cell lines: whereas MIA PaCa-2 cells are classified as glycolytic, the PANC-1 cells are classified as lipogenic and may therefore respond differently to liposome exposure.[69] However, the exact nature of these metabolic phenotypes in response to radiotherapy and more complex chemoradiotherapy mechanisms are unknown, yet may warrant further investigation.

2.8. Radiotherapy Improves Microtumor Permeability

The ability of radiotherapy to improve tumor permeability has been observed on several occasions, and it has been shown to increase the uptake and efficacy of doxorubicin in mouse models of prostate- and lung cancer.[70] Such effects have been attributed to radiotherapy-induced vascular remodeling, changes in the tumor extracellular matrix architecture, and relieved fluid pressures and solid stress.[70,71] To investigate whether the radiotherapy-enhancing properties of the AuDDT-BPD-OXILs could be leveraged for chemoradiotherapy approaches, the microtumor permeability was investigated on heterotypic microtumors in vitro. Calcein was chosen as a hydrophilic dye with poor cellular uptake, and its ability to penetrate into radiotherapy-treated microtumors was quantified using confocal laser scanning microscopy by applying a relatively thin focal plane of 22.5 µm. For MIA PaCa-2+HPSC microtumors, the AuDDT-BPD-OXILs appeared to disturb the microtumor integrity, which was exacerbated by radiotherapy. The microtumors were disturbed following treatment, with a large aura of cells radiating out from a dense tumor core (**Figure 6B**). Calcein penetration occurred along the microtumor periphery upon exposure to AuDDT-BPD-OXILs, and significantly higher overall calcein emission was observed in microtumors exposed to radiotherapy at 4 Gy, but not at 16 Gy (Figure 6A). Analysis of calcein emission profiles across the microtumors revealed substantial increases in calcein emission in the low-density cell aura, with little calcein emission from the denser tumor core (Figure 6B). In the 16 Gy-treated microtumors, similar observations of increased calcein emission from the microtumor periphery were made, yet the overall calcein intensity did not reach statistical significance (Figure 6A,B). It is interesting to note that the microtumor packing was largely restored when investigated 7 days after radiotherapy (Figure 5A; Figure S6, Supporting Information). In PANC-1+HPSC microtumors, radiotherapy appeared more effective at increasing tumor permeability as quantified using the mean calcein emission intensities (Figure 6C). Analysis of cross sections confirms the observations in the MIA PaCa-2+HPSC microtumors, in which the calcein penetration is particularly elevated in the cancer peripheries (Figure 6D). In the PANC-1+HPSC microtumors, the effect of AuDDT-BPD OXILs on microtumor permeability was not significantly different to that of radiotherapy alone.

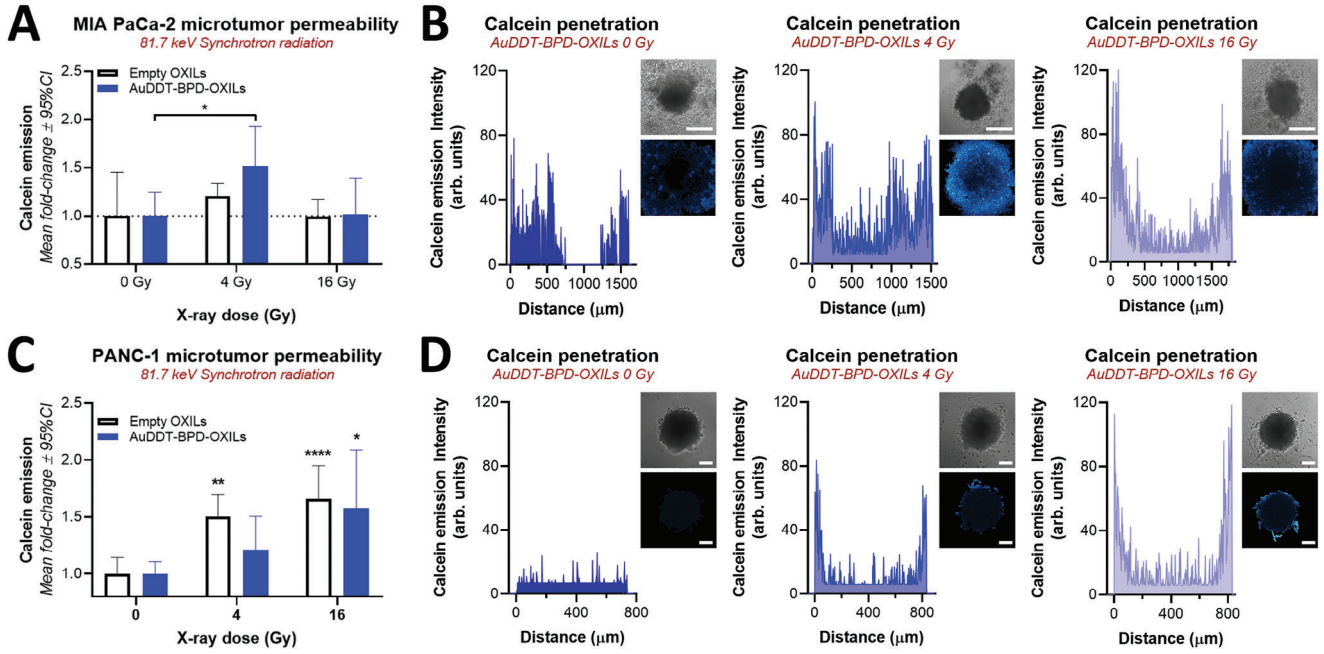

Figure 6. AuDDT-OXILs improve oxaliplatin-chemoradiotherapy outcomes in MIA PaCa-2+HPSC pancreatic microtumors. A) Mean calcein emission from MIA PaCa-2+HPSC microtumors following radiotherapy. B) Cross sections of MIA PaCa-2+HPSC microtumors, displaying the calcein fluorescence emission, after 0 Gy (B) and 4 Gy (C) monochromatic irradiation (81.7 keV), acquired using confocal fluorescence microscopy (22.5 μm focal plane). Scalebar = 500 μm. C) Mean calcein emission from PANC-1+HPSC microtumors following radiotherapy. D) Cross sections of PANC-1+HPSC microtumors, displaying the calcein fluorescence emission, after 0 Gy (B), 4 Gy (C), and 16 Gy (D) radiotherapy delivered using monochromatic X-rays (81.7 keV), acquired using confocal fluorescence microscopy (22.5 μm focal plane). Scalebar = 250 μm. Data passed normality tests (panel A: Kolmogorov–Smirnov test, Panel C: Pearson–Omnibus test), and statistical analyses were performed using a One-way ANOVA and Sidak's post-hoc test for multiple comparisons.

Overall, it appears that radiotherapy increases tumor permeability by perturbing cell–cell interactions at the tumor periphery, but it is not significantly influenced by AuDDT-BPD-OXILs. Increased tumor permeability is typically attributed to increased vascular permeability and interstitial pressures, but the findings presented here obtained in non-vascularized microtumors suggest that there are also cellular or subcellular mechanisms at play. These findings are somewhat contradictory to radiobiological investigations that have reported upregulation of cell–cell and cell–matrix adhesion proteins such as integrins and cadherins.[72] On the other hand, excessive ROS production by photodynamic approaches has been associated with immediate reductions in integrins and extracellular matrix proteins.[18] Further studies toward the kinetics of tumor permeabilization, and the immediate and long-term regulations of such tumor integrity markers could shed light on how to best exploit these priming effects for chemoradiotherapy. Indeed, observations of microtumor morphology post-irradiation suggest that radiotherapy causes rapid disintegration of MIA PaCa-2+HPSC cultures after 24 h, but this effect was better observed after 7 days for the more condensed PANC-1+HPSC microtumors (Figure S6, Supporting Information). Although the influence of oxaliplatin on the mechanobiological properties of cancer tissues remains unexplored, the disintegration of the PANC-1+HPSC microtumors by oxaliplatin chemoradiotherapy as observed here (Figure S5A, Supporting Information) may present a promising alternative approach to achieve increased cancer permeability.

2.9. AuDDT-BPD-OXILs Accumulate in Orthotopic Pancreatic Cancer In Vivo

The encouraging in vitro findings inspired in vivo biodistribution studies in orthotopic models of pancreatic cancer. As BPD is known to leach from liposomes in the presence of blood plasma components,[73–75] AuDDT-BPD-OXILs were prepared in which BPD was replaced by a lipid anchored-BPD (BPD-PC) that has similar photochemical and optical properties.[21,76] Upon intravenous injection of the liposomes, the biodistribution of the OXILs could be tracked in vivo by fluorescence imaging and 3D fluorescence tomography by benefiting from the fluorescent properties of BPD-PC (**Figure** 7A,B). Fluorescence imaging revealed a prominent accumulation of the OXILs in cancer tissues (Figure 7C), with a tumor: skin ratio of 1.1 ± 0.2, a tumor: muscle ration of 5.8 ± 1.9, and a tumor: pancreas ratio of 2.7 ± 0.8 at 24 h. Uptake by the liver and spleen was also substantial at 5 h post-administration, as is expected and previously reported.[77–79] Systemic clearance was indicated by significant reductions in BPD-PC emissions from these organs as detected 24 h post-administration. However, the BPD-PC emission did not diminish in the orthotopic tumor between 5 h and 24 h post-administration, indicating that the OXILs are well retained in the tumor microenvironment (Figure 7C). No renal elimination of the OXILs was observed as the bladder could not clearly be discerned from images of the mice in the supine position (Figure S7, Supporting Information). At 24 h post-irradiation, the intestines displayed BPD-emission in vivo, yet this was not

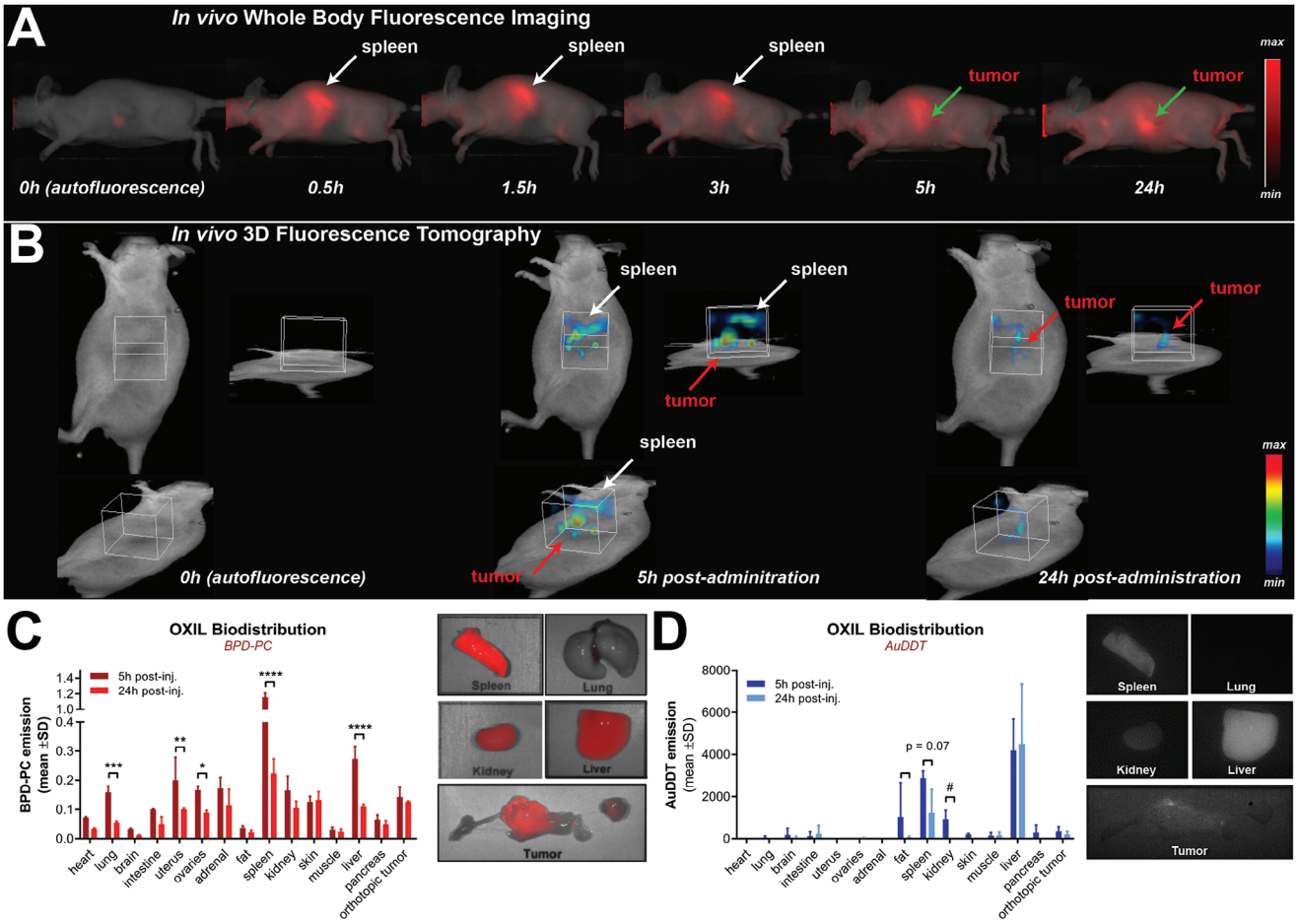

Figure 7. Differential biodistribution of lipid-anchored BPD and AuDDT when administered as AuDDT-BPD-OXILs. A) Side views of a representative mouse that received AUDDT-BPD-OXILs via i.v. injection, obtained by the whole body in vivo fluorescence imaging at different timepoints. B) The accumulation of AuDDT-BPD-OXILs in cancer tissues was imaged using 3D fluorescence tomography zoomed into the area containing the spleen, pancreas, and tumor. C) Distribution of OXILS based on the fluorescence of BPD-PC determined at 5 h post-administration (dark red) or 24 h post-administration (bright red). D) Distribution of AuDDT determined by SWIR fluorescence imaging at 5 h post-administration (dark blue) or 24 h post-administration (light blue). Data from panels C and D are from $N = 3$ per timepoint, and statistical analysis was performed with a One-way ANOVA and Sidak's multiple comparison's test (asterisks) or a student's *t*-test (hashtags).

observed in empty intestines ex vivo (Figure S7, Supporting Information). The elimination of the OXILs thus appears to occur via the hepatic-intestinal route. The accumulation of the OXILs in the spleen could be problematic for translational studies in mice, in which the pancreas/pancreatic tumor is located in very close proximity to the spleen. However, state-of-the-art preclinical irradiation systems are available in which multiple irradiation beams can be placed with a highly precise cross section over the cancer tissues. As such, CT-guided beam placement can avoid the irradiation of the liver and spleen.[80]

In addition to tracking the biodistribution of the AuDDT-BPD-OXILs based on the NIR-fluorescence of BPD-PC, their biodistribution was also investigated using the SWIR emission of the AuDDT ex vivo. Quantification of the AuDDT fluorescence emission resulted in biodistribution profiles that were notably different from that of BPD-PC (Figure 7D). AuDDT fluorescence was predominantly detected in the spleen, liver, and kidneys 5 h post-administration. While the AuDDT was cleared from the spleen and kidneys at 24 h post-injection, the AuDDT emission from the liver remained high. A minor but temporally stable emission of AuDDT was detected in the orthotopic pancreatic tumors. LIBS, a complementary elemental-imaging approach,[81,82] was unable to spatially detect Au in the cancer tissues (Figure S7B, Supporting Information). These findings were attributed to the low amount of AuDDT within the NLs (0.5 mol%), and the sensitivity of the AuDDT detection methods. In addition, quenching of the AuDDT fluorescence was observed when co-encapsulated with BPD (Figure S1E,F, Supporting Information), indicating that higher AuDDT-BPD-OXIL doses and higher AuDDT: lipid ratios need to be explored to reach detectable and therapeutically sufficient AuDDT concentrations in cancer tissues.

Based on the dissimilar biodistribution profiles of BPD and AuDDT after 5 and 24 h, we hypothesized that an interaction of AuDDT with serum lipoproteins would occur. Indeed, incubation of water-insoluble AuDDT pellets with pure fetal bovine serum at 37 °C resulted in solubilization (Figure S7E, Supporting Information). We have therefore expanded on these studies by including a biodistribution evaluation at 1 h post-administration.

The results, based on BPD-PC fluorescence emission, demonstrate that the liposomes exhibited no notable tumor accumulation at this timepoint, and are primarily sequestered in the spleen and liver (Figure S7C,D, Supporting Information). AuDDT follows the exact same pattern, indicating that AuDDT may still be retained in the nanoliposomes at this timepoint. Taken together our biodistribution findings revealed that, while the nanoliposomes exhibited excellent tumor accumulation after 5 and 24 h post-injection, the AuDDT did not. This hints toward limited retention of the AuDDT within the liposomes, leading to overall poor tumor accumulation.

The simulations, biochemical, and therapeutic effects presented here were of a fundamental nature, for which we leveraged the unique monochromatic properties of synchrotron radiation. The findings warranted further research in a preclinical setting, envisioning to use broad-spectrum small-animal- and clinical X-ray irradiators. Our findings suggest that translational studies toward the radiotherapeutic applications of the AuDDT-BPD-OXILs would be highly insightful and relevant, but only when the limitations of the currently presented approach can be addressed. This would require substantial advancements in liposome- and nanocluster engineering. In this context, this study primarily investigated the use of nanoliposomes containing hydrophobic AuDDT nanoclusters for radiotherapy enhancement. This choice was primarily driven by the prospect of radiotherapy-controlled drug delivery as described in Figure 3, the main benefit being that including the hydrophobic AuDDT within the lipid bilayer leaves an empty aqueous core that can be loaded with hydrophilic cargo. In our study, oxaliplatin was explored as a prime drug candidate based on the findings of Figures 4 and 5. However, various other approaches to load Au nanoclusters in lipid-nanocarriers can be explored for radiotherapy enhancement. The first strategy is the loading of hydrophilic Au nanoclusters in the aqueous core of nanoliposomes. Although classic lipid-film hydration is notorious for its low encapsulation efficiencies of hydrophilic cargoes, the use of cationic peptide-stabilized AuNCs and liposomes containing ionizable lipids can yield promising loading efficiencies of 26–42%.[83] Reverse-phase evaporation is another attractive method, for which AuNC loading efficiencies of 40–100% have been reported.[84–87] A second approach is the use of micelles that can load significantly higher amounts of hydrophobic Au nanoclusters, as demonstrated for poly(ethyl methacrylate) nanoparticles,[88] and lipodisks.[89] A third approach is the use of lipid-conjugated AuNCs, as reported for distearoyl-glycerol-phosphine-Au_{55}.[90] These approaches warrant further investigations as the radiotherapeutic potential of such approaches may strongly depend on the excipients used to formulate the Au nanoclusters.

3. Conclusion

This study characterized the radiotherapeutic properties of NLs that were supplemented with high-Z elements. To this end, AuDDT nanoclusters were included within the lipid bilayer of NLs, which augmented ROS generation and radiotherapy outcomes in 3D pancreatic microtumors. The PEGylated OXILs displayed effective tumor accumulation in an in vivo orthotopic mouse model of pancreatic cancer. These findings point toward exciting opportunities to advance the development of radioresponsive NLs. First, alternative nanoliposome fabrication strategies should be developed that can load high-Z elements more homogeneously within the NLs. Second, such fabrication processes should allow for the inclusion of high-Z elements at higher molar ratios, which should translate to a higher radiocatalytic potential. Third, as the lipids appear to be active bystanders in these radiocatalytic NLs, the bioengineering of novel lipid formulations may aid in identifying suitable nanoliposome compositions to prevent liposome fusion/instability. Last, efforts to anchor the high-Z elements within the lipid bilayer may hold significant promise for the translation of high-Z metalated NLs, as the radiocatalytic components will benefit fully from the long-circulating abilities of the NLs and their ability to accumulate in cancer tissues due to the EPR effect. Upon overcoming the challenges identified in this study, high-Z metalated NLs may become a promising and versatile tool in the radiotherapeutic arsenal. Applications may range from radiation dose-enhancement, augmenting the enhanced permeability and retention effect in cancer tissues, and enabling radiotherapy-controlled drug delivery. Altogether such advances may pave the way to safer and more effective chemoradiotherapy strategies.

4. Experimental Section

Chemicals and Reagents: Hydrophobic gold nanoclusters (AuNCs) stabilized using dodecanethiol (AuDDT) were prepared and imaged by transmission electron microscopy as described previously.[88,91] AuDDT was suspended in $CHCl_3$ at a concentration of 3.5 mg Au mL. Phospholipids 1,2-distearoylpalmitoyl-sn-glycero-3-phosphocholine (DSPC), 1,2-dioleoyl-sn-glycero-3-phosphoethanolamine (DOPE), *N*-(Carbonyl-methoxypolyethylene-glycol-2000)-1,2-distearoyl-sn-glycero-3-phosphoethanolamine (DSPE-PEG). 1,2-Dilinoleoyl-sn-glycero-3-phosphoethanolamine (DLinPE) and 1,2-dioleoyl-sn-glycero-3-phosphatidylcholine (DOPC) were purchased from Avanti Polar Lipids (Alabaster AL, USA), and cholesterol was from Sigma-Aldrich (Merck, Darmstad, Germany). Calcein, verteporfin/benzoporphyrin derivative (BPD, >94%), Sephadex G50 fine, nitrogen gas, 1-ethyl-3-(3-dimethylaminopropyl) carbodiimide (EDC), 4-dimethylaminopyridine (DMAP), *N,N*-diisopropylethylamine (DIPEA) and (DCM) were acquired from Sigma-Aldrich (Merck). 18:0 BPD-phosphocholine (BPD-PC) was synthesized from 18:0 lyso-PC (Avanti Polar Lipids) as described before.[21]

Nanoliposome Preparation and Characterization: Oxidation-responsive liposomes (OXILs) were prepared using the lipid-film hydration method: lipid films supplemented with AuDDT and/or BPD(-PC) were prepared using vacuum centrifugation (Genevac miVac centrifugal concentrator, 30 °C, 4 h minimum), hydrated in phosphate-buffered saline (PBS, Gibco), and sonicated at 37 kHz for 15 min at 60 °C (Elmasonic p30, Elma Schmidbauer GmbH, Singen, Germany), until a clear solution was obtained. Typical working solutions were prepared at a 5 mM total lipid concentration. Following preparation, liposomes were stored at 4 °C under N_2 gas. Any AuDDT aggregates were removed by centrifugation (60 s, 1000 rcf). All liposomes were characterized using dynamic-/electrophoretic light scattering spectroscopy for size, polydispersity, particle number, and zeta-potential (Malvern Panalytic Zetasizer Ultra Red, Malvern, UK).

To characterize the encapsulation efficiency of AuDDT and the nanoliposome, short-wave infrared (SWIR) fluorescence spectroscopy was performed using a SWIR spectrometer from Wasatch (870–1700 nm; InGaAs Hamamatsu 512 pixels; 6 nm resolution; $f = 1.3$; high pass filter at 830 nm) coupled with an optical fiber ($\varnothing = 300$ µm, NA = 0.39) and using an 808 nm laser (120 mW cm^{-2}) as excitation source. Diluted samples were measured in a quartz microcuvette (12.5 × 4.5 × 45 mm) with a 2 mm light path and spectra were recorded in the Wasatch software

at high gain and 500 ms acquisition time (average of 10 scans). The size, polydispersity index, and zeta potential, of the AuDDT liposomes were determined by electrophoretic light scattering spectroscopy and dynamic light scattering using the Zetasizer Ultra Red (Malvern Panalytical, Malvern, UK). Nanoparticle tracking analysis was performed with a NanoSight NS300 (Malvern Panalytical). To quantify the AuDDT encapsulation efficiency, 200 µL aliquots of AuDDT-NLs were desiccated by vacuum centrifugation and reconstituted in 200 µL $CHCl_3$. The resulting fluorescence spectra were similar to that of native AuDDT in $CHCl_3$ (Figure S1A, Supporting Information), and the encapsulation efficiency was quantified by solving a standard curve based on the integrated fluorescence intensity (area under the curve 886–1703 nm) (Figure S1B, Supporting Information).

Cryo-Electron Microscopy: NLs with a formulation of DOPE:DSPC:DSPE-PEG: Cholesterol (24:24:4:48 mol%) were prepared as described before, and concentrated by ultrafiltration for 45 min at 3000 rcf using 15 mL Amicon filters (30 kDa MWCO, Sigma Aldrich, France). The initial sample was 0.5 mL of 20 mM NLs, and 0.25 mL of NLs at 40 mM final lipid concentrations were stored at 4 °C after purged with N_2 gas (Messer CANgas, Sigma-Aldrich). Samples were prepared by applying 3 µL to glow-discharged 1.2/1.3 hole sized C-Flat holey copper grids with a carbon foil (300 mesh) and plunged frozen in liquid ethane using a Vitrobot Mark IV (Thermo Fisher Scientific) (4 s blot time, blot force -14). The sample was observed at the beamline CM01 of the European Synchrotron Radiation Facility (Grenoble, France[92]) with a Titan Krios G3 (Thermo Fisher Scientific) operating at 300 kV equipped with an energy filter (Bioquantum LS/967, AMETEK) (slit width of 20 eV). Images were recorded on a K3 direct electron detector (AMETEK) in counting mode with EPU (Thermo Fisher Scientific). Movies were acquired at a nominal magnification of x105000 (0.839 Å $pixel^{-1}$ at the camera level) with a total dose of ≈55 e^- $Å^{-1}$[2] distributed over 40 frames. The defocus of the images varied between −1.5 and −3.0 µm. Movies were drift-corrected using MotionCor2[93] and the resulting micrographs were then used for interpreting liposomes.

The CryoTEM images were used to evaluate the efficiency of AuDDT-NL loading. More than 20 images were selected for NLs containing either 0, 0.2, 0.5, and 2 mol% AuDDT. For each subset, the liposomes were first classified by morphology—unilamellar, multilamellar, or fused—and their numbers quantified. Then the occurrence of gold nanoclusters was counted, both across the entire liposome population and within each morphological category. Smaller nanoclusters were counted individually, while aggregated clusters were counted as larger units based on their size and aggregation state.

Cryo-Electron Tomography: The grid of 0.2 mol% AuDTT prepared for cryo-EM (section above) was used for cryo-electron tomography imaging in CM01. Tilt series were collected at a magnification of 33000X in super-resolution counting mode corresponding to a pixel size of 1.38 Å. Movies were aligned using Motioncor2 and binned twice yielding a final pixel size of 2.76 Å. Alignment of tilt series and tomogram reconstruction were performed using AreTomo within the image processing pipeline for electron cryo-tomography in RELION-5.[94]

Small-Angle X-Ray Scattering Spectroscopy (SAXS): Small-angle X-ray scattering (SAXS) measurements were conducted at the SWING beamline of the SOLEIL synchrotron (Saint-Aubin, France). The liposome samples were irradiated using an X-ray beam with an energy of 12 keV, with the detector positioned 6 m from the sample. Data were collected using the EigerX4 M detector (Dectris Ltd, Switzerland), covering a momentum transfer range of $q \approx 0.001064 - 0.1848$ $Å^{-1}$. Where q is defined as $q = (4\pi \sin\vartheta)/\lambda$, with ϑ as the scattering angle and λ the X-ray wavelength. A total of 40 µL of the liposome solution was aliquoted into each well of a V-bottom 96-well plate, which was then placed into the automated sample loader for SAXS data collection. Each sample underwent 48 image acquisitions with an exposure time of 990 ms per image, plus an additional 10 ms of dead time between exposures.

The 2D SAXS data were converted to 1D scattering intensity curves using Foxtrot software (available from https://www.synchrotron-soleil.fr/en/beamlines/swing). Background scattering from the PBS buffer was subtracted to isolate the scattering contribution of the liposomes. The radius of gyration (Rg) was estimated using the command-line program AUTORG of ATSAS software, which applies the Guinier approximation ($I(s) = I(0)\exp(-s^2Rg^2/3)$) to the small-angle scattering data. The Rg value was obtained from the best linear fit of the Guinier plot, which represents $\ln[I(s)]$ versus s^2, within the range of scattering vectors where the condition $sRg \leq 1.0–1.3$ is met.[95]

Geant4 Monte Carlo Simulations: The spectra of secondary electrons that were generated upon the interaction of Au with monochromatic X-rays were simulated using Geant4 (version 4.10.1, patch 01),[96] using the Livermore low energy package as previously described.[97,98] Briefly, a rod of Au (1 nm^2 area and 1 mm long) placed in a vacuum was simulated and was virtually exposed to 1.10^6 photons of monochromatic X-rays (at energies of 79.7 and 81.7 keV, that is, 1 keV above and below the Au K-edge) that were targeted to the center of the 1 nm^2 surface. All secondary particles (electrons and photons) generated upon the interaction between the incoming X-rays and the material were collected by a virtual detector placed symmetrically around the Au rod.

X-Ray Irradiation: X-ray irradiations were performed using monochromatic synchrotron radiation at the ID17 Biomedical beamline of the European Synchrotron Radiation Facility. The beam was operated in multi-bunch mode (unless otherwise indicated), with monochromatic X-rays (energy bandwidth < 100 eV) tuned between 30 and 100 keV using a silicium double crystal Laue-Laue fixed-exit monochromator. The dose-rate was 4.4 mGy s^{-1} mA^{-1}. The irradiations were given via a beam that was 100 mm wide and 1 mm-high. Multi-wells plates were inclined at a 30° angle with respect to the X-ray beam. The plate was irradiated vertically up to a height of 8 cm via a moving stage. The correct X-ray dose was determined by calculating the number of scans based on dose-rate calibrations using an ion chamber (UNIDOS PTW 31 002, Freiburg, Germany).

Detection of Radiation-Induced Generation of Reactive Oxygen Species: ROS generation by X-ray irradiations was assessed using the hydroxyl radical sensor aminophenyl fluorescein (APF, Merck). Reaction mixtures of 100 µL were prepared, containing 10 µM APF and various NLs at a final lipid concentration of 100 µM. The fluorescence of the reaction mixtures was measured before and after X-ray irradiation at $\lambda_{exc.}$ 485 ± 10 nm, $\lambda_{em.}$ 520 ± 20 nm (Clariostar multiplate reader, BMG Labtech). All data was normalized to the background fluorescence measured at 0 Gy. To assay radiation-controlled lipid oxidation, cargo release assays were performed on various AuDDT-OXIL variants that were loaded with a self-quenching solution of calcein (53 mM calcein, 180 mM NaCl, pH 7.4, 0.282 osmol kg^{-1}[99]). Reaction mixtures of 100 µL were prepared, in which the various liposomes were diluted to a final concentration of 100 µM in PBS. The calcein emission was measured before and after X-ray irradiation and after lysis in 0.1% Triton X-100 (final concentration) at $\lambda_{exc.}$ 485 ± 10 nm, $\lambda_{em.}$ 520 ± 20 nm. All data was normalized to the maximum calcein emission following Triton X-100 addition. The synergy index for APF oxidation between AuDDT-NLs, BPD-NLs, and AuDDT-BPD-NLs was calculated using $(Eff_{A+B} - 1)/((Eff_A - 1) + (Eff_B - 1))$. The fraction effect for ROS production was used by normalizing the value of the APF emission with the maximum APF emission value of each individual dose, and the mean synergy index was reported as a mean across all doses. Additional experiments using 420 nm light instead of X-rays were performed in a similar fashion, with the use of a Lumidox Gen II, 96-well LED-arrays (Analytical Sales and Services, Flanders, NJ, USA), operating at 78.13 mW cm^{-2} and applying radiant exposures between 0.5–48 J cm^{-2}.

Toxicity Evaluation on Non-Cancer Cells: The toxicity of empty NLs, BPD-NLs, AuDDT-NLs, and AuDDT-BPD-NLs were investigated on the HPSC and on the renal HEK 293 cell line (American Type Culture Collection). 5×10^3 HPSC cells per well or 10^4 HEK 293 cells per well were plated into 96-well plates (Corning, Corning NY, USA). After an overnight growth, the cells were incubated with increased concentrations of the NLs formulations (up to 2,5 mM) for 24 h. Cell viability was determined using MTS viability assay (CellTiter 96 AQueous One Solution Cell Proliferation Assay, Promega, Madison, WI, USA) for the HPSC cells and MTT viability assay (Merck, Germany) for the HEK 293 cells, following the manufacturer's instructions.

Establishment of Heterotypic 3D Cultures of Pancreatic Cancer: Human pancreatic cancer cell lines PANC-1 (CRL-1469), and MIA PaCa-2

(CRL-1420) pancreatic cancer cell lines were obtained from the American Type Culture Collection and used between passages 2–30. Human pancreatic stellate cells (HPSC) were obtained from ScienCell (San Diego, CA), and used between passages 2–15. All cells were cultured in DMEM containing 5 mM Glutamax, supplemented with 10% (v/v) fetal bovine serum and 1% (v/v) penicillin/streptomycin. For suspended heterotypic spheroid cultures, 5×10^3 cancer cells were co-cultured with 5×10^3 HPSC in 96-well U-bottom ultra-low adhesion plates (Corning, Corning NY, USA). Dense cancer spheroids were formed within 24 h of culturing.

Quantification of Microtumor Permeability: Quantitative assessment of tumor permeability was studied in heterotypic spheroids, using calcein as a drug analog. Cells were seeded on day 1. On culture day 4 the spheroids were incubated with 500 µM of AuDDT-OXILs. After a 4 h incubation period, the spheroids were irradiated at either 0, 4, or 16 Gy, using 81.7 keV monochromatic X-rays. Directly, afterward, 50 µM calcein was added to each well. After 24 h of incubation, the spheroids were gently washed twice with PBS and re-immersed in a culture medium. The uptake of calcein by the spheroids was performed by quantitative confocal fluorescence microscopy (Zeiss LSM510, using a 10× objective (EC Plan-Neofluar, NA 0.3) at λ_{ex} 488 nm and λ_{em} 500–540 nm. Global calcein uptake was determined by automated image analysis,[100,101] which quantified the total fluorescence emission of calcein collected from the spheroids. Spheroids that were out of focus were excluded from the analysis. The calcein penetration depth was quantified by plotting the calcein fluorescence emission as a histogram across the microtumors.

Quantification of Treatment Efficacies: The radiotherapeutic properties of the NLs were assessed on 4 day-old spheroids, which were incubated for 4 h with 500 µM AuDDT-OXILs (final lipid concentration; 2.5 µM Au), and irradiated with X-rays at the indicated doses and X-ray energies. Irradiations were performed in 16-bunch mode at 0.1 mGy s^{-1}. Oxaliplatin (100 µM) was added immediately thereafter. Treatment efficacies were determined on culture day 14 using live (calcein AM) and dead (propidium iodide) staining, confocal fluorescence microscopy, and quantitative image analysis, as described previously.[100,102] MIA PaCa-2+HPSC microtumors were imaged using a 5× objective (N-Acroplan, NA 0.16), whereas PANC-1+HPSc microtumors were imaged using a 10× objective (EC Plan-Neofluar, NA 0.3).

In Vivo Biodistribution: All animal experiments were in accordance with the application for authorization of animal experiments submitted to the Ministry of Research and the Ethics Committee (APAFIS #39533-2022111814174926 v4). Female, 6-week-old NMRI nude mice (Janvier Labs) and underwent surgery under isoflurane anesthesia to expose the spleen and pancreas. Subsequently, 1×10^6 PANC-1-pGL4 cells, suspended in 200 µL of Matrigel (Corning) were injected in the pancreas. Clinical follow-up consisted of behavior observation and monitoring of animal weight, performed 2–3 times a week. On day 35 after implantation, bioluminescence imaging was performed: Animals received 300 µL of *D*-luciferin (Promega) i.p. at 10 mg mL^{-1} and were imaged 5–10 min post luciferin injection (IVIS Kinetic, PerkinElmer). Animals were evenly distributed in treatment groups according to tumor signal.

AuDDT-BPD-OXILs containing 0.8 moL% 18:0 BPD-PC and 0.5 mol% AuDDT were prepared at a lipid concentration of 6.25 mM and a final BPD concentration of 50 µM, which was selected based on previous work.[21] All OXILs underwent size-extrusion using 200 nm Whatman Anotop filters (Merck). Following randomization on day 35 post-implantation (tumor size 100 mm^3), mice bearing orthotopic PDAC received 200 µL (0.36 mg BPD kg^{-1}) of the AuDDT-BPD-OXIL solution via tail-vein injection under isoflurane anesthesia.

In vivo, whole-body fluorescence imaging (right and left sides, prone and supine positions) was performed prior to injection, and at 30 min, 90 min, 3 h, 5 h (6 mice), and 24 h (3 mice) post-injection under isoflurane anesthesia (Pearl Trilogy, LI-COR Biosciences GmbH, Bad Homburg, Germany) using λ_{ex} = 685 nm, λ_{em} = 700–720 nm. Animals were additionally imaged using 3D fluorescence tomography using a custom-built setup, followed by 3D CT (VivaCT, Scanco Medical, Wangen–Brüttisellen, Switzerland). Animals were humanely euthanized by cervical dislocation under gas anesthesia after 5 or 24 h post-injection. Organs were isolated and separately imaged using bioluminescence and fluorescence imaging (Li-Cor Pearl Trilogy) to quantify the distribution of BPD and BPD-PC. To image the biodistribution of the AuDDT delivered via AuDDT-BPD-OXILs, organs were imaged *ex vivo* using a custom-built shortwave infrared imaging setup (InGaAs Nirvana 640ST camera, Princeton), a 50 mm lens from Navitar (NA = 1.4), and a long pass filter at 1064 nm (Semrock), and excitation by 808 nm laser (120 mW cm^{-2}) with a 200 ms acquisition time.

Laser-Induced Breakdown Spectroscopy (LIBS): LIBS elemental imaging was performed on ex vivo tumor cryosections (10 µm) analyzed at room temperature, using a setup previously described.[103,104] Briefly, a Nd: YAG laser (Centurion, Quantel, Villejust, France, 1064 nm, pulse duration = 8 ns, repetition rate = 100 Hz) was focused on the target through a microscope objective (LMM-15X-P01, Thorlabs, Newton NJ, USA). Samples were placed on a 3D motorized stage and were scanned pixel by pixel, with a lateral resolution of 25 µm and an energy of 2 mJ per pulse. Each pixel was a result of a single shot and no average or accumulation was performed. A flow of 0.8 L min^{-1} of argon gas was directed on the plasma region during the whole experiment. The plasma emission was collected by two spectrometers coupled to ICCD cameras (iStar, Andor, Belfast, UK). The first spectrometer (Shamrock 303, Andor) directly collected the plasma light through an entrance slit of 35 µm and a grating of 1800 lines mm^{-1} (300 nm blaze), to ensure a high resolution in the UV for detecting both intense line of phosphorus at 213.6 and 214.9 nm. On the other hand, the second spectrometer (Shamrock 500, Andor) was coupled with a bundle of optic fibers, an entrance slit of 50 µm and a grating of 600 lines mm^{-1} (300 nm blaze), allowing the detection of numerous elemental transitions, such as magnesium at 285.2 nm and gold at 267.6 nm. The delay and gate detection for both detectors were set to 1 and 5 µs respectively, with a gain of 1500. The acquisition and data analysis were performed using a custom-developed LabVIEW software (National Instruments, Austin TX, USA).

Inductively-Coupled Plasma Mass Spectroscopy (ICP-MS) Gold Concentration Quantification: NLs formulations composed of DOPE:DSPC:DSPE-PEG: Cholesterol (24:24:4:48 mol%) containing either 0.5 mol% AuDDT only or the combination of 0.5 mol% AuDDT + 0.8 mol% BPD were prepared as previously described. Afterward, a known volume of the prepared formulation was dried using vacuum centrifugation (Genevac miVac centrifugal concentrator, 40 °C, 24 h minimum) to get NLs pellets. Thereafter, aqua regia (1:3 molar ratio of HNO_3 (67% wt, Merck, Germany) and HCl (35% wt, Merck, Germany), respectively) was added to the NLS pellets and left for overnight incubation. On the next day, the digestion was completed through heating at 70 °C for 1 h. Before the ICP-MS measurements, the digested samples were diluted with deionized water to a final volume of 10 mL and transferred to the ICP-MS tubes. A calibration curve of gold concentrations up to 1000 ppb (µg L^{-1}) was obtained using the analytical gold standard TraceCERT, 1 g L^{-1} Au in hydrochloric acid (Merck, Germany). The NexION 1000 ICP-MS instrument (Perkin Elmer, Shelton, CT, USA) at the University Technical Institute of Chemistry (Grenoble Alpes University) was used for the measurements.

Statistical Analyses: Statistical analyses were performed in Graphpad Prism 7 (San Diego, CA, USA). All data were normally distributed according to D'Agostino-Pearson omnibus tests. For ROS production and liposome-cargo release assays, data were fitted using dose-response fits (agonist vs response (three parameters)), and statistically compared using an extra-sum-of-squares F-test. Intergroup differences were analyzed using a one-way ANOVA and Tukey's post hoc test for multiple comparisons (indicated using asterisks), or using a student's *t*-test when indicated (indicated using hashtags). Statistical significance was indicated with single symbols ($p \leq 0.05$), double symbols ($p \leq 0.01$), triple symbols ($p \leq 0.005$), or quadruple symbols ($p \leq 0.001$).

Supporting Information

Supporting Information is available from the Wiley Online Library or from the author.

Acknowledgements

N.M.C.G. and T.L.C. contributed equally to this work. This research was funded by the Phospholipid Research Center, Heidelberg, Germany (MAB-2020- 080/1- 1), the Institut National de la Santé et de la Recherche Médicale (INSERM, Paris France), and the Grenoble Enterprises Against Cancer (GEFLUC, Grenoble, France). In addition, this research was supported by the European Union M.B: (ERC STG, RADIOCONTROL, 101078392) and A-L.B. (ERC STG, RADIANCE, 101116304). Views and opinions expressed were, however, those of the authors only and did not necessarily reflect those of the European Union or the European Research Council Executive Agency. Neither the European Union nor the granting authority could be held responsible for them. X.L.G. gratefully acknowledges funding by the Agence National de la Recherche (ANR-20CE09-0039-01). The authors additionally acknowledge the European Synchrotron Radiation Facility for the provision of beam time on ID17A (MD-1216, MD-1294, MD-1320, and MD-1325), and CM01 (inhouse research). The authors thank the Microcell core facility of the Institute for Advanced Biosciences (UGA, Inserm U1209, CNRS 5309). This facility belongs to the IBISA-ISdV platform, a member of the national infrastructure France-BioImaging supported by the French National Research Agency (ANR-10-INBS-04). The authors further express their gratitude to Aurelien Thureau (Synchrotron Soleil, Saint Auban, France), Pau Bernado (Centre de Biologie Structurale, CNRS UMR 5048, INSERM U 1054, University of Montpellier, France), and Daniel Hermida Merino (European Synchrotron Radiation Facility, Grenoble, France) for their aid with the SAXS measurements and data interpretation.

Conflict of Interest

The authors declare no conflict of interest.

Data Availability Statement

The data that support the findings of this study are available from the corresponding author upon reasonable request.

Keywords

3D culture models, chemoradiotherapy, monochromatic synchrotron radiation, oxaliplatin, lipid nanotechnology, pancreatic cancer, radiation therapy, radiotherapy-controlled drug delivery, tumor permeability

Received: March 29, 2024
Revised: September 21, 2024
Published online:

[1] J. E. Chaft, A. Rimner, W. Weder, C. G. Azzoli, M. G. Kris, T. Cascone, *Nat. Rev. Clin. Oncol.* **2021**, *18*, 547.
[2] D. E. Johnson, B. Burtness, C. R. Leemans, V. W. Y. Lui, J. E. Bauman, J. R. Grandis, *Nat. Rev. Dis. Primers* **2020**, *6*, 92.
[3] R. S., K. Sa, H. Cl, K. Rk, G. Gj, *Nat. Rev. Clin. Oncol.* **2018**, *15*, 310.
[4] S. W. L. de Geus, M. F. Eskander, G. G. Kasumova, S. C. Ng, T. S. Kent, J. D. Mancias, M. P. Callery, A. Mahadevan, J. F. Tseng, *Cancer* **2017**, *123*, 4158.
[5] S. Moningi, A. S. Dholakia, S. P. Raman, A. Blackford, J. L. Cameron, D. T. Le, A. M. C. De Jesus-Acosta, A. Hacker-Prietz, L. M. Rosati, R. K. Assadi, S. Dipasquale, T. M. Pawlik, L. Zheng, M. J. Weiss, D. A. Laheru, C. L. Wolfgang, J. M. Herman, *Ann. Surg. Oncol.* **2015**, *22*, 2352.
[6] M. Suker, J. J. Nuyttens, B. Groot Koerkamp, F. A. L. M. Eskens, C. H. van Eijck, *J. Surg. Oncol.* **2018**, *118*, 1021.
[7] R. D. Peixoto, M. Ho, D. J. Renouf, H. J. Lim, S. Gill, J. Y. Ruan, W. Y. Cheung, *Am. J. Clin. Oncol.* **2017**, *40*, 507.
[8] Y. Chen, K. M. McAndrews, R. Kalluri, *Nat. Rev. Clin. Oncol.* **2021**, *18*, 792.
[9] A. N. Hosein, R. A. Brekken, A. Maitra, *Nat. Rev. Gastroenterol. Hepatol.* **2020**, *17*, 487.
[10] D. Hanahan, R. A. Weinberg, *Cell* **2011**, *144*, 646.
[11] P. P. Adiseshaiah, R. M. Crist, S. S. Hook, S. E. McNeil, *Nat. Rev. Clin. Oncol.* **2016**, *13*, 750.
[12] H. E. Barker, J. T. E. Paget, A. A. Khan, K. J. Harrington, *Nat. Rev. Cancer* **2015**, *15*, 409.
[13] H.-C. Huang, I. Rizvi, J. Liu, S. Anbil, A. Kalra, H. Lee, Y. Baglo, N. Paz, D. Hayden, S. Pereira, B. W. Pogue, J. Fitzgerald, T. Hasan, *Cancer Res.* **2018**, *78*, 558.
[14] G. Obaid, S. Bano, H. Thomsen, S. Callaghan, N. Shah, J. W. R. Swain, W. Jin, X. Ding, C. G. Cameron, S. A. McFarland, J. Wu, M. Vangel, S. Stoilova-McPhie, J. Zhao, M. Mino-Kenudson, C. Lin, T. Hasan, *Adv. Sci.* **2022**, *9*, 2104594.
[15] D. Luo, K. A. Carter, J. Geng, X. He, J. F. Lovell, *Mol. Pharm.* **2018**, *15*, 3682.
[16] D. Luo, K. A. Carter, E. A. G. Molins, N. L. Straubinger, J. Geng, S. Shao, W. J. Jusko, R. M. Straubinger, J. F. Lovell, *J. Controlled Release* **2019**, *297*, 39.
[17] M. Broekgaarden, R. Weijer, T. M. van Gulik, M. R. Hamblin, M. Heger, *Cancer Metastasis Rev.* **2015**, *34*, 643.
[18] C. Gutierrez, N. M., N. Pujol-Solé, Q. Arifi, J.-L. Coll, T. Clainche, M. Broekgaarden, *Cancer Metastasis Rev.* **2022**, *41*, 899.
[19] J. W. Snyder, W. R. Greco, D. A. Bellnier, L. Vaughan, B. W. Henderson, *Cancer Res.* **2003**, *63*, 8126.
[20] T. Araki, K. Ogawara, H. Suzuki, R. Kawai, T. Watanabe, T. Ono, K. Higaki, *J. Controlled Release* **2015**, *200*, 106.
[21] G. Obaid, S. Bano, S. Mallidi, M. Broekgaarden, J. Kuriakose, Z. Silber, A.-L. Bulin, Y. Wang, Z. Mai, W. Jin, D. Simeone, T. Hasan, *Nano Lett.* **2019**, *19*, 7573.
[22] B. Q. Spring, R. Bryan Sears, L. Z. Zheng, Z. Mai, R. Watanabe, M. E. Sherwood, D. A. Schoenfeld, B. W. Pogue, S. P. Pereira, E. Villa, T. Hasan, *Nat. Nanotechnol.* **2016**, *11*, 378.
[23] M. M. Kim, A. Darafsheh, *Photochem. Photobiol.* **2020**, *96*, 280.
[24] J. M. Borras, M. Barton, C. Grau, J. Corral, R. Verhoeven, V. Lemmens, L. van Eycken, K. Henau, M. Primic-Zakelj, P. Strojan, M. Trojanowski, A. Dyzmann-Sroka, A. Kubiak, C. Gasparotto, N. Defourny, J. Malicki, P. Dunscombe, M. Coffey, Y. Lievens, *Radiother. Oncol.* **2015**, *116*, 45.
[25] J.-L. Ravanat, T. Douki, *Radiat. Phys. Chem.* **2016**, *128*, 92.
[26] X-Ray Mass Attenuation Coefficients NIST https://www.nist.gov/pml/x-ray-mass-attenuation-coefficients (accessed: July 2021).
[27] M. Misawa, J. Takahashi, *Nanomedicine* **2011**, *7*, 604.
[28] J. D. Carter, N. N. Cheng, Y. Qu, G. D. Suarez, T. Guo, *J. Phys. Chem. B* **2007**, *111*, 11622.
[29] J. F. Hainfeld, D. N. Slatkin, H. M. Smilowitz, *Phys. Med. Biol.* **2004**, *49*, N309.
[30] M. Broekgaarden, A.-L. Bulin, E. Porret, B. Musnier, B. Chovelon, C. Ravelet, L. Sancey, H. Elleaume, P. Hainaut, J.-L. Coll, X. L. Guével, *Nanoscale* **2020**, *12*, 6959.
[31] G. Liang, X. Jin, S. Zhang, D. Xing, *Biomaterials* **2017**, *144*, 95.
[32] D. Luo, X. Wang, S. Zeng, G. Ramamurthy, C. Burda, J. P. Basilion, *Small* **2019**, *15*, e1900968.
[33] X.-D. Zhang, J. Chen, Z. Luo, D. Wu, X. Shen, S.-S. Song, Y.-M. Sun, P.-X. Liu, J. Zhao, S. Huo, S. Fan, F. Fan, X.-J. Liang, J. Xie, *Adv. Healthcare Mater.* **2014**, *3*, 133.
[34] X. Le Guével, M. Henry, V. Motto-Ros, E. Longo, M. I. Montañez, F. Pelascini, O. de La Rochefoucauld, P. Zeitoun, J.-L. Coll, V. Josserand, L. Sancey, *Nanoscale* **2018**, *10*, 18657.
[35] J. Fang, H. Nakamura, *Adv. Drug Delivery Rev.* **2011**, *63*, 136.

[36] R. Jin, C. Zeng, M. Zhou, Y. Chen, *Chem. Rev.* **2016**, *116*, 10346.
[37] M. R. Rasch, Y. Yu, C. Bosoy, B. W. Goodfellow, B. A. Korgel, *Langmuir* **2012**, *28*, 12971.
[38] M. R. Rasch, E. Rossinyol, J. L. Hueso, B. W. Goodfellow, J. Arbiol, B. A. Korgel, *Nano Lett.* **2010**, *10*, 3733.
[39] M. R. Rasch, C. A. Bosoy, Y. Yu, B. A. Korgel, *Langmuir* **2012**, *28*, 15160.
[40] M. R. Preiss, A. Hart, C. Kitchens, G. D. Bothun, *J. Phys. Chem. B* **2017**, *121*, 5040.
[41] X. Kang, H. Chong, M. Zhu, *Nanoscale* **2018**, *10*, 10758.
[42] A. S. Apolline, L. Haye, A. Alhalabi, S. Mornet, A. Reisch, X. L. Guével, L. Cognet, *ChemRxiv* **2023**.
[43] S. Chakraborty, A. Abbasi, G. D. Bothun, M. Nagao, C. L. Kitchens, *Langmuir* **2018**, *34*, 13416.
[44] G. Von White, Y. Chen, J. Roder-Hanna, G. D. Bothun, C. L. Kitchens, *ACS Nano* **2012**, *6*, 4678.
[45] D. Radziuk, D. Grigoriev, W. Zhang, D. Su, H. Möhwald, D. Shchukin, *J. Phys. Chem. C* **2010**, *114*, 1835.
[46] D. V. Radziuk, W. Zhang, D. Shchukin, H. Möhwald, *Small* **2010**, *6*, 545.
[47] P. R. Cullis, B. de Kruijff, *Biochim. Biophys. Acta* **1979**, *559*, 399.
[48] A. L. Bailey, P. R. Cullis, In *Current Topics in Membranes, Epand, R. M., Ed., Lipid Polymorphism and Membrane Properties*, Academic Press, Cambridge, MA, USA **1997**, *44*, pp 359.
[49] M. J. Blandamer, B. Briggs, P. M. Cullis, B. J. Rawlings, J. B. F. N. Engberts, *Phys. Chem. Chem. Phys.* **2003**, *5*, 5309.
[50] R. Lipowsky, R. Dimova, *J. Phys.: Condens. Matter* **2002**, *15*, S31.
[51] D. J. A. Crommelin, P. van Hoogevest, G. Storm, *J. Controlled Release* **2020**, *318*, 256.
[52] Auger Electron Spectroscopy Methods https://serc.carleton.edu/msu_nanotech/methods/aes.html (accessed: March 2024).
[53] W. Deng, K. J. McKelvey, A. Guller, A. Fayzullin, J. M. Campbell, S. Clement, A. Habibalahi, Z. Wargocka, L. Liang, C. Shen, V. M. Howell, A. F. Engel, E. M. Goldys, *ACS Cent. Sci.* **2020**, *6*, 715.
[54] J. Axelsson, S. C. Davis, D. J. Gladstone, B. W. Pogue, *Med. Phys.* **2011**, *38*, 4127.
[55] B. W. Pogue, B. C. Wilson, *J. Biomed. Opt.* **2018**, *23*, 121610.
[56] P. Worthington, P. Hambright, R. F. X. Williams, J. Reid, C. Burnham, A. Shamim, J. Turay, D. M. Bell, R. Kirkland, R. G. Little, N. Datta-Gupta, U. Eisner, *J. Inorg. Biochem.* **1980**, *12*, 281.
[57] S. J. McMahon, W. B. Hyland, M. F. Muir, J. A. Coulter, S. Jain, K. T. Butterworth, G. Schettino, G. R. Dickson, A. R. Hounsell, J. M. O'Sullivan, K. M. Prise, D. G. Hirst, F. J. Currell, *Sci. Rep.* **2011**, *1*, 18.
[58] D. C. Litzinger, L. Huang, *Biochim. Biophys. Acta* **1992**, *1113*, 201.
[59] D. Luo, N. Li, K. A. Carter, C. Lin, J. Geng, S. Shao, W.-C. Huang, Y. Qin, G. E. Atilla-Gokcumen, J. F. Lovell, *Small* **2016**, *12*, 3039.
[60] M. Broekgaarden, S. Anbil, A.-L. Bulin, G. Obaid, Z. Mai, Y. Baglo, I. Rizvi, T. Hasan, *Biomaterials* **2019**, *222*, 119421.
[61] A.-L. Bulin, M. Broekgaarden, D. Simeone, T. Hasan, *Oncotarget* **2019**, *10*, 2625.
[62] S. Her, D. A. Jaffray, C. Allen, *Adv. Drug Delivery Rev.* **2017**, *109*, 84.
[63] A. E. O'Connor, W. M. Gallagher, A. T. Byrne, *Photochem. Photobiol.* **2009**, *85*, 1053.
[64] K. Plaetzer, B. Krammer, J. Berlanda, F. Berr, T. Kiesslich, *Lasers Med. Sci.* **2009**, *24*, 259.
[65] Z. A. Wainberg, D. Melisi, T. Macarulla, R. Pazo Cid, S. R. Chandana, C. De La Fouchardière, A. Dean, I. Kiss, W. J. Lee, T. O. Goetze, E. Van Cutsem, A. S. Paulson, T. Bekaii-Saab, S. Pant, R. A. Hubner, Z. Xiao, H. Chen, F. Benzaghou, E. M. O'Reilly, *Lancet* **2023**, *402*, 1272.
[66] L. A. Daamen, P. J. Parikh, W. A. Hall, *Semin. Radiat. Oncol.* **2024**, *34*, 23.
[67] L. Di Cesare Mannelli, M. Zanardelli, P. Failli, C. Ghelardini, *Free Radical Biol. Med.* **2013**, *61*, 143.
[68] S. Afzal, S. A. Jensen, J. B. Sørensen, T. Henriksen, A. Weimann, H. E. Poulsen, *Cancer Chemother. Pharmacol.* **2012**, *69*, 301.
[69] A. Daemen, D. Peterson, N. Sahu, R. McCord, X. Du, B. Liu, K. Kowanetz, R. Hong, J. Moffat, M. Gao, A. Boudreau, R. Mroue, L. Corson, T. O'Brien, J. Qing, D. Sampath, M. Merchant, R. Yauch, G. Manning, J. Settleman, G. Hatzivassiliou, M. Evangelista, *Proc. Natl. Acad. Sci. U. S. A.* **2015**, *112*, E4410.
[70] V. Potiron, K. Clément-Colmou, E. Jouglar, M. Pietri, S. Chiavassa, G. Delpon, F. Paris, S. Supiot, *Cancer Lett.* **2019**, *457*, 1.
[71] J. Wang, Y. Han, Y. Li, F. Zhang, M. Cai, X. Zhang, J. Chen, C. Ji, J. Ma, F. Xu, *Small Methods* **2022**, *6*, 2200570.
[72] R. G. Baluna, T. Y. Eng, C. R. Thomas, *Radiat. Res.* **2006**, *166*, 819.
[73] K. A. Carter, S. Shao, M. I. Hoopes, D. Luo, B. Ahsan, V. M. Grigoryants, W. Song, H. Huang, G. Zhang, R. K. Pandey, J. Geng, B. A. Pfeifer, C. P. Scholes, J. Ortega, M. Karttunen, J. F. Lovell, *Nat. Commun.* **2014**, *5*, 3546.
[74] H.-C. Huang, S. Mallidi, J. Liu, C.-T. Chiang, Z. Mai, R. Goldschmidt, N. Ebrahim-Zadeh, I. Rizvi, T. Hasan, *Cancer Res.* **2016**, *76*, 1066.
[75] A. J. Versluis, P. C. Rensen, M. E. Kuipers, W. G. Love, P. W. Taylor, *J. Photochem. Photobiol. B* **1994**, *23*, 141.
[76] G. Obaid, W. Jin, S. Bano, D. Kessel, T. Hasan, *Photochem. Photobiol.* **2019**, *95*, 364.
[77] D. C. Litzinger, L. Huang, *Biochim. Biophys. Acta, Lipids Lipid Metab.* **1992**, *1127*, 249.
[78] V. D. Awasthi, D. Garcia, B. A. Goins, W. T. Phillips, *Int. J. Pharm.* **2003**, *253*, 121.
[79] T. M. Allen, C. Hansen, F. Martin, C. Redemann, A. Yau-Young, *Biochim. Biophys. Acta, Biomembr.* **1991**, *1066*, 29.
[80] S. Dobiasch, S. Kampfer, K. Steiger, D. Schilling, J. C. Fischer, T. E. Schmid, W. Weichert, J. J. Wilkens, S. E. Combs, *Cancers* **2021**, *13*, 5656.
[81] V. Gardette, L. Sancey, M. Leprince, L. Gaté, F. Cosnier, C. Seidel, S. Valentino, F. Pelascini, J.-L. Coll, M. Péoc'h, V. Scolan, F. Paysant, V. Bonneterre, C. Dujardin, B. Busser, *Small Sci.* **2024**, *4*, 2300307.
[82] V. Gardette, V. Motto-Ros, C. Alvarez-Llamas, L. Sancey, L. Duponchel, B. Busser, *Anal. Chem.* **2023**, *95*, 49.
[83] E. Butera, A. Dupont, A. Aimé, S. Ducarre, R. M. Chiechio, P. Even-Hernandez, A. Contino, G. Maccarone, C. Ravel, V. I.n Marchi, *ACS Appl. Mater. Interfaces* **2024**, *16*, 21643.
[84] L. Paasonen, T. Laaksonen, C. Johans, M. Yliperttula, K. Kontturi, A. Urtti, *J. Controlled Release* **2007**, *122*, 86.
[85] G. A. Dichello, T. Fukuda, T. Maekawa, R. L. D. Whitby, S. V. Mikhalovsky, M. Alavijeh, A. S. Pannala, D. K. Sarker, *Eur. J. Pharm. Sci.* **2017**, *105*, 55.
[86] R. M. Chiechio, S. Ducarre, C. Marets, A. Dupont, P. Even-Hernandez, X. Pinson, S. Dutertre, F. Artzner, P. Musumeci, C. Ravel, M. J. L. Faro, V. Marchi, *Nanomaterials* **2022**, *12*, 3875.
[87] R. M. Chiechio, S. Ducarre, G. Moulin, A. Dupont, C. Marets, P. Even-Hernandez, F. Artzner, P. Musumeci, G. Franzò, C. Ravel, M. J. LoFaro, V. Marchi, *J. Phys. Chem. Lett.* **2022**, *13*, 6935.
[88] I. Moskalevska, V. Faure, L. Haye, M. Mercey-Ressejac, A. K. Dey, B. Chovelon, L. K. Soro, L. J. Charbonnière, A. Reisch, A. S. Klymchenko, P. N. Marche, J.-L. M Coll, Z. Jilkova, X. le Guével, *Int. J. Pharm.* **2023**, *630*, 122439.
[89] A. T. Rad, Y. Bao, H.-S. Jang, Y. Xia, H. Sharma, E. E. Dormidontova, J. Zhao, J. Arora, V. T. John, B. Z. Tang, T. Dainese, A. Hariri, J. V. Jokerst, F. Maran, M.-P. Nieh, *Adv. Funct. Mater.* **2021**, *31*, 2009750.
[90] J. Sot, S. A. Mendanha-Neto, J. V. Busto, A. B. García-Arribas, S. Li, S. W. Burgess, W. A. Shaw, D. Gil-Carton, F. M. Goñi, A. Alonso, *Chem. Phys. Lipids* **2019**, *218*, 40.
[91] L. Haye, P. I. Diriwari, A. Alhalabi, T. Gallavardin, A. Combes, A. S. Klymchenko, N. Hildebrandt, X. Le Guével, A. Reisch, *Adv. Opt. Mater.* **2023**, *11*, 2201474.

[92] E. Kandiah, T. Giraud, A. de Maria Antolinos, F. Dobias, G. Effantin, D. Flot, M. Hons, G. Schoehn, J. Susini, O. Svensson, G. A. Leonard, C. Mueller-Dieckmann, *Acta Crystallogr., Sect. D: Struct. Biol.* **2019**, *75*, 528.
[93] S. Q. Zheng, E. Palovcak, J.-P. Armache, K. A. Verba, Y. Cheng, D. A. Agard, *Nat. Methods* **2017**, *14*, 331.
[94] A. Burt, B. Toader, R. Warshamanage, A. von Kügelgen, E. Pyle, J. Zivanov, D. Kimanius, T. A. M. Bharat, S. H. W. Scheres, *FEBS Open Bio* **2024**, https://febs.onlinelibrary.wiley.com/action/showCitFormats?doi=10.1002%2F2211-5463.13873.
[95] M. V. Petoukhov, P. V. Konarev, A. G. Kikhney, D. I. Svergun, *J. Appl. Cryst.* **2007**, *40*, s223.
[96] S. Agostinelli, J. Allison, K. Amako, J. Apostolakis, H. Araujo, P. Arce, M. Asai, D. Axen, S. Banerjee, G. Barrand, F. Behner, L. Bellagamba, J. Boudreau, L. Broglia, A. Brunengo, H. Burkhardt, S. Chauvie, J. Chuma, R. Chytracek, G. Cooperman, G. Cosmo, P. Degtyarenko, A. Dell'Acqua, G. Depaola, D. Dietrich, R. Enami, A. Feliciello, C. Ferguson, H. Fesefeldt, G. Folger, et al., *Nucl. Instrum. Methods Phys. Res., Sect. A* **2003**, *506*, 250.
[97] A.-L. Bulin, A. Vasil'ev, A. Belsky, D. Amans, G. Ledoux, C. Dujardin, *Nanoscale* **2015**, *7*, 5744.
[98] A.-L. Bulin, M. Broekgaarden, F. Chaput, V. Baisamy, J. Garrevoet, B. Busser, D. Brueckner, A. Youssef, J.-L. Ravanat, C. Dujardin, V. Motto-Ros, F. Lerouge, S. Bohic, L. Sancey, H. Elleaume, *Adv. Sci.* **2020**, *7*, 2001675.
[99] M. Broekgaarden, A. I. P. M. de Kroon, T. M. Van Gulik, M. Heger, *Curr. Med. Chem.* **2013**, *21*, 377.
[100] A.-L. Bulin, M. Broekgaarden, T. Hasan, *Sci. Rep.* **2017**, *7*, 16645.
[101] T. Le Clainche, N. M. Carigga Gutierrez, N. Pujol-Solé, J.-L. Coll, M. Broekgaarden, *Onco* **2022**, *2*, 19.
[102] A.-L. Bulin, M. Broekgaarden, T. Hasan, *Methods Mol. Biol.* **2022**, *2451*, 59.
[103] B. Busser, S. Moncayo, F. Trichard, V. Bonneterre, N. Pinel, F. Pelascini, P. Dugourd, J.-L. Coll, M. D'Incan, J. Charles, V. Motto-Ros, L. Sancey, *Mod. Pathol.* **2018**, *31*, 378.
[104] B. Busser, A.-L. Bulin, V. Gardette, H. Elleaume, F. Pelascini, A. Bouron, V. Motto-Ros, L. Sancey, *J. Neurosci. Methods* **2022**, *379*, 109676.